A Conformable Linear Electrode Platform for Impedance Mapping of Soft Tissue Interfaces

Aditti Ramsisaria

CMU-RI-TR-25-59

July 2025

The Robotics Institute
School of Computer Science
Carnegie Mellon University
Pittsburgh, PA

Thesis Committee:
Cameron Riviere, *co-chair*
Carmel Majidi, *co-chair*
Gary Fedder
Akhil Padmanabha

Submitted in partial fulfillment of the requirements for the degree of Master of Science in Robotics.

To my parents and brother—for instilling in me the drive to imagine, to build, and for standing beside me with unwavering support through it all

Abstract

Soft electrode arrays capable of conforming to complex anatomical surfaces are vital for emerging biomedical sensing technologies. They are particularly relevant in applications requiring large-area, high-resolution mapping. Reducing the time required for such mapping is critical to minimize overall procedure duration and improve clinical efficiency. However, the electrical performance of such systems under mechanical deformation remains poorly understood. This thesis presents a novel soft electrode line architecture for large-area sensing on non-planar surfaces inspired by the contours of the natural human anatomy. The system features a modular structure of alternating copper electrodes and silicone tubing, internally bridged by stainless steel wires—enabling geometric adaptability and electrical continuity while maintaining a manufacturable, low-profile form factor. Mechanical modeling revealed that internal wires dominate flexural stiffness, limiting curvature before exceeding physiological force thresholds or inducing plastic deformation. These constraints guided the design of conductive tissue-phantoms for impedance testing under realistic curvature and pressure. Electrochemical impedance spectroscopy (EIS) was used to assess performance across four representative geometries and loading states. Results showed that curvature increased impedance and reduced capacitive response due to diminished double-layer formation and altered field distribution, while pressure improved contact and lowered impedance. Equivalent circuit modeling captured the dominant spectral trends across geometries and enabled systematic comparison of how geometry affects interfacial and bulk electrical properties, revealing consistent trade-offs between contact uniformity and field confinement. Together, these results establish a blueprint for embedding deformable electrodes in constrained biological environments without sacrificing signal fidelity. The insights gained offer valuable design guidance for future systems requiring both mechanical adaptability and electrochemical reliability, and lay the groundwork for next-generation conformable biosensing platforms.

Acknowledgments

I would like to express my deepest gratitude to my advisors, Prof. Cameron Riviere and Prof. Carmel Majidi, for their mentorship, guidance, and continuous support throughout this project. Their insights and encouragement were invaluable at every stage—from initial ideation to final execution. I am also grateful to my thesis committee members, Prof. Gary Fedder and Akhil Padmanabha, for their thoughtful feedback.

I would like to sincerely thank Dr. Samir Saba at UPMC for his clinical insights and generous discussions, which helped me better understand the practical limitations of existing biomedical sensing technologies and refine the research direction accordingly.

My heartfelt thanks go to Christina Patterson, Dinesh Patel, Michael Vinciguerra, and David Quinn from the Soft Machines Lab—not only for their technical expertise and troubleshooting help, but for their constant encouragement, patience, and generosity over the past two years. Their willingness to teach and collaborate made the lab feel like a genuinely supportive community, and I'm deeply grateful for everything they've contributed to both this project and my growth as a researcher.

Contents

List of Figures

List of Tables

Chapter 1

Introduction

1.1 Overview

Biomedical sensors are critical tools for interfacing with the human body, enabling diagnostic and therapeutic monitoring through electrical, chemical, and mechanical signals. Traditionally, their design has favored mechanical rigidity and precise geometry to achieve high-fidelity signal acquisition. While this has served well in many extracorporeal and surface-level diagnostic tools, such rigidity poses a substantial limitation when sensors are required to conform to complex, soft, or internal biological environments [13, 16, 23]. Many clinically relevant regions—such as the inner walls of organs, convoluted vascular or cardiac structures, or dynamically deforming tissues—remain difficult to sense accurately due to geometrical inaccessibility or mechanical mismatch between rigid probes and compliant tissue. In response to this critical challenge, there has been a paradigm shift toward developing soft, conformable, and geometrically adaptive sensors capable of reaching and adhering to previously inaccessible anatomical regions [9, 13, 14, 16, 22, 23].

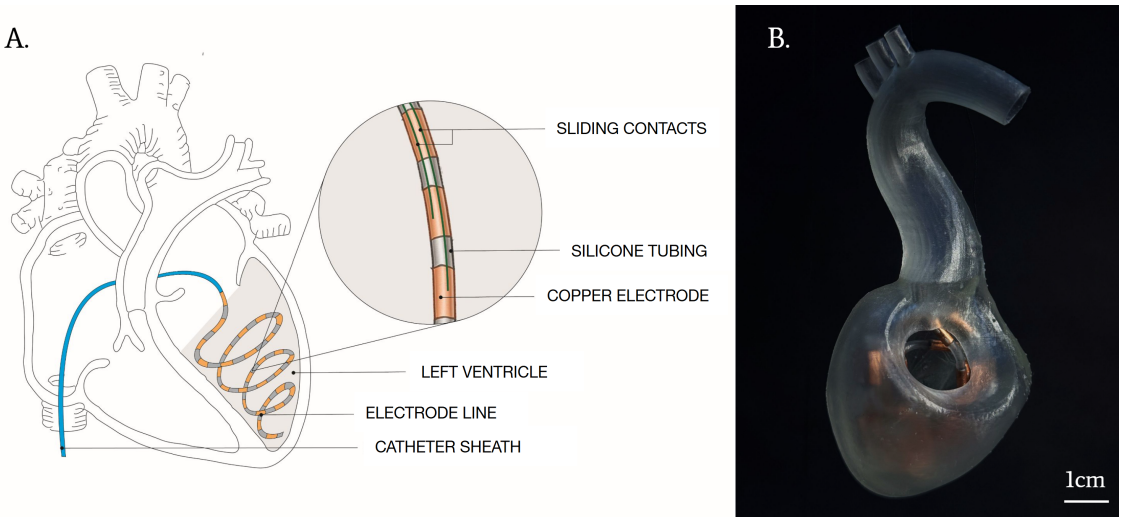

Figure 1.1: *Concept and deployment of a conformable, linear electrode line.* **A.** Schematic of the electrode line coiled within the left ventricle, with an inset showing copper electrodes embedded in silicone tubing with sliding contacts for distributed sensing. **B.** Prototype deployed in a 3D-printed left ventricle phantom, demonstrating conformability to complex endocardial geometry.

This project presents a **novel, linearly distributed soft electrode array designed for mechanical compliance, scalable fabrication, and modular electrical configuration**. Unlike traditional electrode systems that assume fixed positioning and rigid-body insertion, this system embraces flexibility in both structure and configuration—allowing it to achieve dense spatial coverage for bipolar measurements through a minimal number of electrical channels. Initially motivated by the limitations of traditional cardiac electroanatomical mapping catheters [19], this sensor platform generalizes the need for accessible, minimally invasive, and mechanically adaptive sensing tools across a wide range of biomedical and industrial applications. One illustrative application is shown in Figure 1.1, where the electrode line is deployed within a 3D-printed cardiac phantom to demonstrate its ability to conform to endocardial geometry—highlighting the broader potential of this platform in interfacing with organ-scale anatomical structures. By enabling conformal access to complex and fragile anatomical regions, such sensors could dramatically improve intraoperative monitoring, minimize the need for repeated insertions, and unlock new possibilities for real-time diagnostics, and personalized treatment strategies.

The central hypothesis of this work is that soft linear electrode arrays—constructed

through a simple, modular fabrication process using off-the-shelf materials—can achieve form factors and electrode configurations suitable for anatomically complex environments. A major goal of the project is to shift the emphasis from merely achieving bioelectrical signal acquisition to simplifying and improving the fabrication processes. Rather than targeting uniform electrical behavior across all conditions, this platform emphasizes geometric adaptability and structural compliance—through passive elasticity alone—enabling sensing in curved or confined spaces that are traditionally inaccessible to rigid probes. To further increase versatility, the system includes a novel sliding-wire interface that enables repositionable electrical access along the electrode line, allowing selective readout without internal routing or embedded electronics.

Mechanical analysis of the electrode line confirms that its flexural rigidity falls within physiologically compatible ranges, supporting its relevance for applications such as organ-surface mapping or intra-cavitary deployment. Through a combination of simulation and experimental testing, I demonstrate that the sensor can conform to straight, looped, convex, and concave geometries and capture curvature-dependent changes in impedance when placed into contact with these surfaces. I also show that this variation can be systematically characterized and interpreted using equivalent circuit models, establishing a foundation for geometry-aware bioelectronic sensing. While this platform is intended to be adaptable across a range of biomedical and industrial settings, the primary design motivations, constraints, and performance parameters for this proof-of-concept iteration are drawn from the specific requirements of cardiac mapping technologies.

To contextualize the system's mechanical performance, I first perform a beam-theory-based bending analysis to identify stiffness regimes appropriate for interfacing with compliant biological substrates. This analysis reveals limits on the minimum achievable bend radius before plastic deformation takes place or contact forces beyond safe limits for cardiac tissue are generated. These findings directly inform the design of phantom geometries used in electrical testing and provide a grounded expectation for how mechanical deformation might influence performance.

A central metric used throughout this study is electrical impedance spectroscopy (EIS), which enables frequency-resolved characterization of the electrical behavior of electrode–tissue interfaces [3, 4, 8, 11, 15, 20, 28]. I first evaluate the impedance

response with increasing contact pressure and in-plane curvature, and then across various 2D and 3D geometries.

Instead of assuming an abstract or purely empirical equivalent circuit, this work adopts a physiologically informed model to interpret how mechanical curvature and geometric embedding affect impedance spectra. The analysis uses the model proposed by Lempka et al. [15], which was originally developed to describe neural interface electrodes. This formulation includes a constant phase element (CPE) and polarization resistance in parallel, in series with a solution resistance and an additional CPE, capturing both the electrode–electrolyte interface and the frequency-dependent dispersion within the surrounding medium. Constant phase elements (CPEs) in this context represent non-ideal capacitive behavior arising from distributed time constants, surface roughness, and spatially heterogeneous contact between the electrode and the conductive phantom material.

Rather than extending the model with additional branches, the same Lempka formulation was applied consistently across all electrode geometries in this work. This approach enables a direct comparison of fitted parameters to assess how changes in contact quality and geometric confinement influence the underlying electrochemical behavior. The analysis highlights which terms in the model are most sensitive to mechanical factors and how they evolve as the electrode transitions from flat to increasingly complex, curved embeddings. The electrode platform presented here thus serves not only as a practical sensing device, but also as a controlled testbed for understanding how deformation shapes impedance spectra through the lens of a widely used, interpretable equivalent circuit framework.

The sensor itself is constructed using a custom fabrication process with off-the-shelf materials: silicone tubing serves as a soft scaffold for copper-based electrodes. A distinguishing feature of this system is the use of two thin stainless-steel sliding wires which are threaded through the lumen of the tubing and act as dynamic contact probes, selectively pressing against internal connections to form reconfigurable electrode pairs. This design supports bipolar impedance measurements with variable spacing, enabling dense scanning without extensive wiring. The result is a sparse-wire, electrode-dense platform that enables rapid spatial scanning without requiring dedicated wiring for each electrode. This sliding-contact approach not only reduces complexity and bulk at the interface level but also introduces a programmable sensing capability that can

adapt to the spatial demands of a particular application.

This architecture is particularly well-suited for non-planar surfaces where spatial conformity is essential. It supports both stretchability and thinness while maintaining robust electrical performance. Moreover, it bypasses the need for complex techniques like photolithography, relying instead on simple, reproducible steps accessible in most lab settings. This makes the sensor a strong candidate for early-stage prototyping.

The project also involves systematic testing of the sensor in application-relevant phantom environments. These include soft gel phantoms (such as agar) to simulate compliant biological tissues [12, 21]. Rather than optimizing for a single task, this work emphasizes understanding generalizable trends—identifying when and how electrode geometry and placement influence electrical behavior. The results support the broader claim that robust soft-electrode platforms must account for spatial deformation and electrochemical model variability in order to achieve reliable sensing in the real world.

The long-term vision of this platform is not confined to a specific sensing modality. While this thesis uses EIS as a proof-of-concept for measurement and mapping, the same hardware architecture could be extended to pressure, electrochemical, temperature, or even stretch sensors by altering the outer contact chemistry or integrating alternative functional materials at the electrode sites. In this sense, the platform serves not only as a finished sensing device but also as a testbed for soft electrode research, where new ideas in material integration, geometry, or contact physics can be prototyped quickly and validated across standardized phantom environments.

This thesis is structured as follows. Chapter 2 outlines the materials, design considerations, and step-by-step fabrication protocol, including its construction and connection strategy. Chapter 3 describes the development of tissue-mimicking phantoms and details the experimental setup used to evaluate the electrical performance of the device. Chapter 4 presents the results of mechanical analysis and Chapter 5 presents the results of impedance spectroscopy experiments, with attention to geometry-dependent trends, as well as the limitations of the system. Finally, Chapter 6 offers concluding remarks on performance, opportunities for improvement, and potential applications in soft robotics and biomedical sensing.

1.2 Related Work

1.2.1 Applications of Linear Electrode Arrays and Impedance-based Sensing

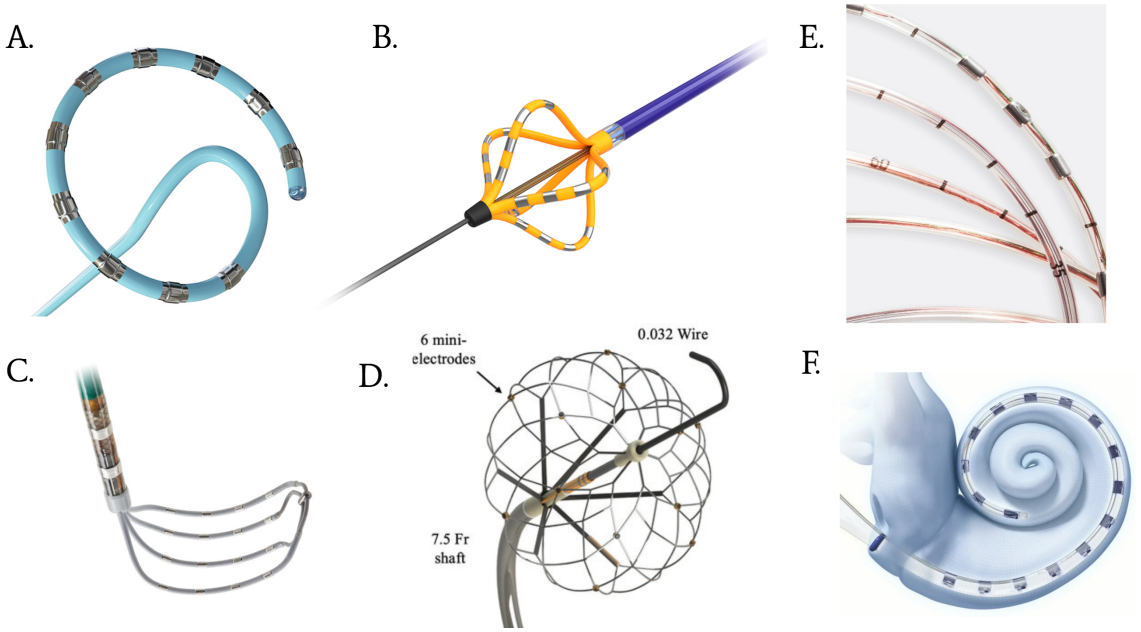

Figure 1.2: *Current commercial technologies.*
A - D: Cardiac Ablation Catheters: **A.** Varipulse™ (J&J Biosense Webster). **B.** FaraPulse™ (Boston Scientific). **C.** HD Advisor Grid™ (Abbott). **D.** Sphere-360™ (Medtronic). **E.** Gastrointestinal tract cathter: ZepHr Impedance and pH Monitoring System (Diversatek). **F.** Cochlear implant: HiFocus SlimJ electrode™ (Advanced Bionics).

Linear electrode arrays have emerged as a robust architecture for spatially resolved sensing across biomedical and non-biomedical domains [7, 17, 18]. Their distributed layout allows for the collection of spatially varying signals, making them particularly useful in applications such as auditory prostheses [7], cardiac mapping [19], and bioimpedance-based diagnostics. However, their widespread adoption is often hindered by application-specific rigidity and structural inflexibility, which makes them poorly suited for anatomically complex or deformable environments.

In cochlear implants, linear arrays are designed to follow the spiral morphology of the cochlea. Studies have shown that the geometry and insertion depth of these arrays significantly influence neural selectivity and speech outcomes [7]. Despite their clinical success, these arrays remain rigid or pre-curved and are not easily tailored to inter-patient variability, making them unsuitable for applications that demand mechanical adaptability.

Cardiac mapping tools like Abbott's Advisor™ HD Grid and Medtronic's Sphere-360™ exemplify the state of the art in multi-electrode platforms. These systems enable broad spatial coverage, but their reliance on rigid catheter geometries, fixed electrode spacing, and complex deployment protocols limits their effectiveness in highly folded or trabeculated heart chambers [19]. The point-by-point mapping strategy and continuous repositioning results in increased procedure times, leading to more complications. Moreover, their inability to dynamically adjust electrode density or contact angle during use creates challenges for resolving fine electrogram details, particularly in regions with recessed or variable topography.

Emerging catheter technologies are addressing mechanical limitations in cardiac environments through improved steerability and force control. Liu et al. propose magnetic soft continuum robots with spatially varying stiffness and magnetization, enabling optimized tip contact forces in constrained vascular spaces [24]. Ali et al. present a mechanically segmented, multi-steerable catheter capable of executing complex, repeatable shapes with four degrees of freedom, offering better adaptability to cardiac anatomy [2]. These innovations reflect a broader shift toward mechanically tunable systems that can outperform rigid electrode arrays in highly curved or patient-specific geometries.

Gastrointestinal probes face similar mechanical challenges. Though impedance sensing has been successfully applied to detect esophageal lesions [25], the rigid construction of catheter-based systems makes them sensitive to gastrointestinal motility, localized deformation, and peristalsis. This can degrade signal quality and introduce variability in electrode-tissue contact, highlighting the need for more compliant and adaptable sensor designs.

Outside the biomedical domain, linear electrode arrays and impedance sensors have found applications in environmental contexts as well. In water quality monitoring, interdigitated platinum electrode arrays have been used to detect copper ions via

pH-induced impedance shifts, offering reagent-free and scalable sensing strategies [5]. In plant science, EIS has been "widely used to estimate plant health, their nutrient status, mineral deficiency, presence of viruses, fruit damages, structural cellular variation during fruit ripening, freeze or chill damages, sensitivity to salinity, and measurement of root system growth in trees" [3].

Flexible impedance arrays have also been proposed in soft robotics and wearables, where they support tactile reconstruction [6], motion tracking [26], and haptic feedback [11]. For instance, lattice-patterned electrodes embedded in elastomeric substrates have been used to enable high-resolution touch mapping through electrical impedance tomography (EIT) [6]. However, these designs often rely on fixed spatial configurations, complex signal reconstruction algorithms, and high-density interconnects, which can hinder their scalability and adaptability in real-time applications. These examples collectively demonstrate that impedance-based sensing offers broad utility across domains. Still, achieving reliable performance in unstructured or variable environments requires electrode architectures that can maintain good contact, adapt geometrically, and minimize wiring complexity.

1.2.2 Emerging Directions in Conformable Sensing

Efforts to address the limitations of rigid and fixed arrays have turned toward stretchable and skin-conforming electronics [13, 16, 23]. Kenry et al. [13] surveyed a wide range of flexible and wearable sensing platforms designed for healthcare and biomedical applications, highlighting the importance of integrating soft materials and mechanical adaptability to achieve continuous physiological monitoring. Their review underscored how mechanical mismatch between sensors and skin or tissue remains a major barrier, motivating the need for intrinsically deformable platforms.

Lim et al. [16] further examined the material and structural design principles necessary for building high-performance skin-like electrodes. They emphasized how material selection—particularly stretchable conductors and elastomers—and microstructural patterning (e.g., serpentine, fractal layouts) can help maintain electrical performance during stretching and bending. Their work demonstrated that combining compliant materials with stress-distributing geometries leads to electrodes that retain fidelity under deformation, but fabrication remains complex and highly specialized.

Vilela et al. [23] focused on flexible sensors for biomedical technology, reviewing advancements in miniaturized systems capable of conforming to soft tissue environments. They highlighted applications ranging from electrophysiology to drug delivery and emphasized the need for scalable manufacturing methods. While these technologies show promise, challenges remain in balancing biocompatibility, sensitivity, and mechanical durability.

For implantable and multifunctional systems, Han et al. developed soft multilayer electrode arrays integrated into catheters for multiplexed sensing and stimulation [10]. Their devices employed serpentine interconnects and stretchable materials to maintain functionality within soft tissue environments. Although these devices show high integration and compliance, they require advanced cleanroom manufacturing, and their electrode layout is still predefined, limiting flexibility in adjusting resolution or layout density during deployment.

Collectively, these works illustrate the growing push toward soft, adaptable bioelectronic systems. However, many existing platforms prioritize skin-conformity or require complex fabrication, motivating the need for modular, low-profile designs that can maintain electrical fidelity under physiological deformation while being manufacturable at scale.

1.2.3 Analytical Models for Electrode Performance

A central challenge in the development of soft, conformable bioimpedance sensors lies in accurately modeling the complex electrical behavior of the electrode–electrolyte interface. This interface exhibits both resistive and capacitive properties, driven by ionic conduction through surrounding tissue and charge accumulation at the electrode surface. These interactions are often captured using equivalent circuit models, which serve as analytical tools to fit impedance spectra and extract interpretable parameters. The goal of such modeling is not only to ensure a good empirical fit, but also to link circuit elements to underlying physical phenomena such as interface quality, contact area, and geometric deformation.

The most basic and widely used model is the parallel resistor–capacitor (RC) circuit, where the resistor represents ionic pathways and the capacitor models the electrical double-layer at the interface. While this model is foundational, its simplicity often

fails to capture the frequency dispersion observed in biological systems—especially under conditions involving tissue heterogeneity, partial wetting, or variable contact pressure. As such, the RC model serves as a baseline but is typically insufficient for describing real-world electrode performance [4, 8].

To address non-ideal capacitive behavior, more advanced models incorporate constant phase elements (CPEs), which represent a distributed range of time constants rather than a single capacitance value. CPEs are particularly effective for modeling the effects of surface roughness, inhomogeneous current distributions, and tissue deformation, all of which contribute to the phase lag observed in experimental impedance spectra. These elements provide a more accurate representation of real-world systems, especially in vivo, where factors such as hydration gradients and tissue deformation introduce non-uniformities in impedance behavior [4, 15, 20].

The ZARC model, which consists of a resistor in parallel with a CPE, is commonly used to model depressed semicircles in Nyquist plots—an indicator of distributed time constants in the interface. This model has proven especially useful in fitting impedance spectra from soft biological plant tissues where ideal capacitive arcs are rarely observed [28].

In the context of neural interfaces, Lempka et al. [15] proposed a physiologically grounded equivalent circuit model shown in Figure 1.3. Their model was developed to capture impedance changes in chronically implanted deep brain stimulation (DBS) electrodes and accounts for both bulk tissue conductivity and dynamic changes in the double-layer due to encapsulation and stimulation history. The proposed model provides a strong conceptual foundation for fitting impedance spectra in compliant or mechanically embedded electrode systems like ours.

The relationship between electrode surface area and impedance behavior has been extensively studied in both engineered and biological systems. Ahmed et al. [1] investigated how electrode geometry influences impedance spectra, demonstrating that surface area directly affects both the magnitude and frequency dependence of observed impedance, particularly through capacitive elements sensitive to double-layer formation. In a biomedical context, Ovadia et al. [20] examined the electrode–tissue interface in the living heart, showing that the equivalent circuit parameters scale with surface area in predictable ways. Building on this foundation, my work evaluates how curvature and contact geometry influence impedance response in soft electrode

arrays.

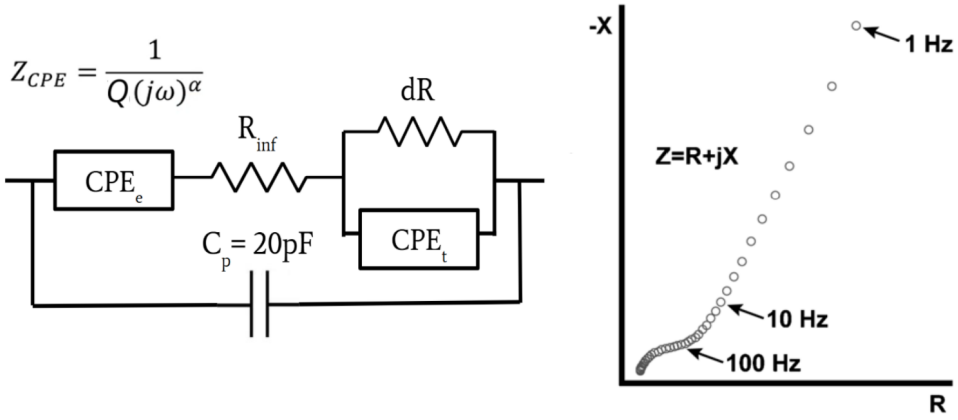

Figure 1.3: *Model proposed by Lempka [15] for deep brain stimulation with platinum/iridium electrodes.*

In this study, I use a single, physiologically motivated equivalent circuit to examine how impedance spectra evolve under changes in electrode geometry and contact. Holding the model structure fixed makes it possible to isolate the influence of deformation on the fitted terms themselves, rather than conflate those effects with changes in model complexity. This consistency allows a clearer comparison between experiments while still retaining enough detail to capture the dominant features of the data.

Here, the equivalent circuit is used less as a generic fitting exercise and more as a lens for interpreting how deformation alters the interface and bulk pathways. Framing the results in this way provides a direct connection between soft electrode mechanics and their electrical behavior, building on previous modeling efforts but shifting the emphasis toward how the same model behaves across very different deployment conditions.

1.2.4 Summary

Across the reviewed literature, several tradeoffs emerge between adaptability, spatial resolution, and fabrication complexity in electrode array design. Rigid systems with

fixed geometries often deliver high-fidelity electrical data but lack the mechanical versatility required for anatomically complex or deformable environments. Meanwhile, soft or conformable systems tend to rely on advanced fabrication methods or dense interconnects, limiting their accessibility and scalability. Analytical models further reveal that key impedance behaviors—particularly those linked to curvature, and partial contact—are underexplored in the context of mechanically embedded soft arrays.

These limitations underscore the need for a new class of electrode systems that combine spatial programmability, mechanical adaptability, and impedance sensitivity within a single architecture. By combining a mechanically tunable architecture with model-informed impedance analysis, this platform offers a foundation for rethinking how soft electrode arrays can be designed, interpreted, and scaled.

Chapter 2

Device Design and Fabrication

This chapter outlines the complete design rationale, materials, and step-by-step fabrication protocol for the linear electrode array developed in this study. Fabrication was performed entirely using off-the-shelf components and standard benchtop tools, making the protocol highly reproducible and adaptable. This chapter serves as a complete guide for replicating the device. Table 2.1 summarizes the materials and equipment used for fabricating the device. Figure 2.1 illustrates the device architecture and fabrication steps. Table 2.2 summarizes the design parameters used to fabricate the device components.

2.1 Tubing and Electrode Preparation

Fabrication began by cutting the silicone tubing to a standard length of 55 cm, which accommodated $\sim$ 50 electrodes with electrodes spaced 1 cm from each other (center to center) while leaving room at both ends for handling and wire routing. Using a digital caliper and fine-point marker, marks were made at the required intervals along the tubing to designate electrode positions.

Both gauges of copper ferrules were cut into 6 mm segments and the lip was removed using a dremel. The copper segments were then deburred using a metal file and sandpaper to ensure smooth insertion. Each prepared segment of the 22 AWG copper ferrules was lubricated with a small amount of silicone oil and gently pressure-fit into the lumen at the marked positions.

Material/Equipment	**Vendor**	**Purpose**
Silicone Tubing (ID: 1 mm, OD: 2 mm)	Quickun	Flexible backbone of electrode line; soft and conformable
Copper Ferrules (14 AWG, 22 AWG)	Ferrules Direct	22 AWG: Inner electrical contact, 14 AWG: Outer electrical contact; conductive with consistent dimensions
Silicone Oil	Sigma-Aldrich	Lubricating ferrules for easy insertion
Silver Conductive Epoxy (8331S - 2-part)	MG Chemicals	Electro-mechanical connection; strong adhesion, low resistivity
PTFE-coated Stainless Steel Wire (CGWX-0100-72)	Component Supply	Sliding contact probes; PTFE coating reduces friction and wear
Acrylic glue (GSE-T7000)	Otriek	Securing contact probes to each other; flexible adhesive
Mini Dremel	HARDELL	Cutting copper ferrules into 6mm electrodes; enables precise, repeatable cuts
Needle tip (19AWG)	McMaster Carr	Cutting holes into tubing; provides clean, consistent perforations
3mL Syringe	BH Supplies	Epoxy deposition; small volume allows controlled application
Metal file	Generic Supplier	Filing electrodes; improves electrical contact and removes burrs
Sandpaper	Generic Supplier	Filing electrodes; fine tuning of surface finish for better epoxy adhesion
Isopropyl Alcohol (IPA)	PTI Process Chemicals	Cleaning residue

Table 2.1: *Materials and equipment used in the fabrication of the proposed device, with notes on selection rationale.*

This was done by using a stiffer copper wire of similar gauge as a plunger to push the ferrules into the correct positions (see Figure 2.1 C). Due to the high friction between the silicone tubing and the copper wire, the wire was pre-lubricated with silicone oil as well. Since the outer diameter of the ferrules was slightly bigger than the tubing inner diameter, the stretchability of the silicone lent itself to get a tight fit.

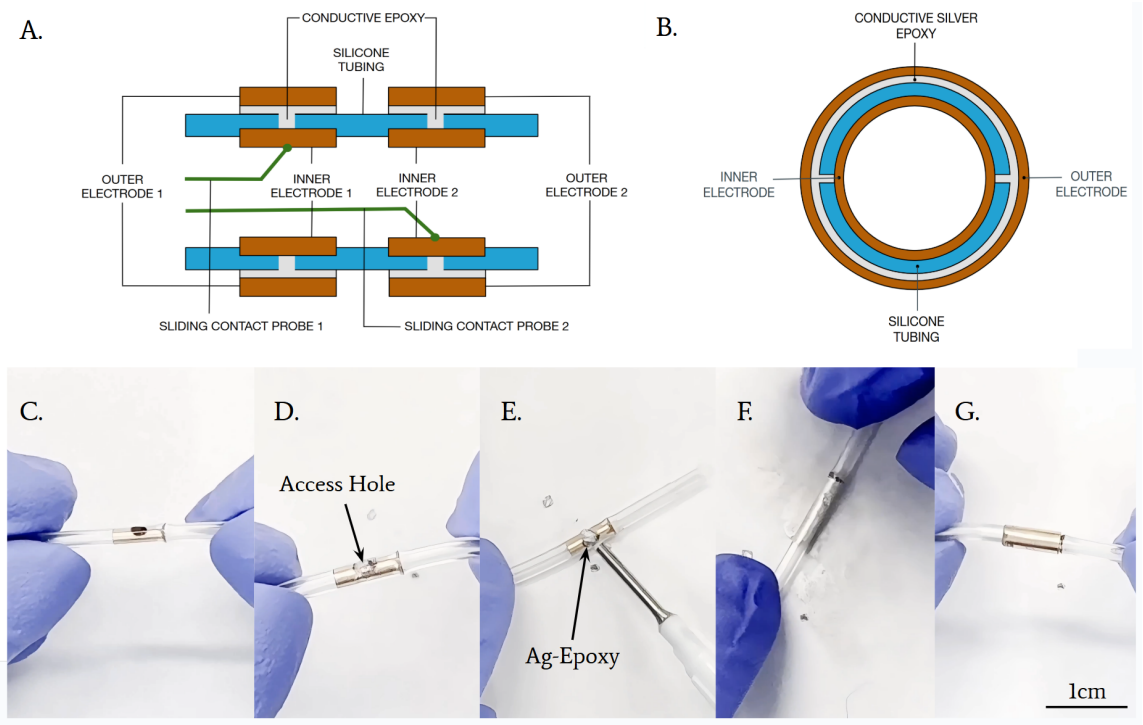

Figure 2.1: *Electrode line architecture and fabrication steps.*
A. Longitudinal schematic of the electrode line. **B.** Cross-sectional view illustrating the coaxial arrangement of the inner and outer electrodes within the tubing. **C–G.** Stepwise fabrication process: **C.** Insertion of inner electrodes into tubing, **D.** Access holes made with needle tip, **E.** Application of conductive silver epoxy to establish connection, **F.** Distribution of excess epoxy **G.** Assembly showing completed outer electrode interface.

2.2 Electrode Access Holes and Epoxy Deposition

After inserting all ferrules, a 19 AWG needle tip was used to create two small holes (see Figure 2.1 D) on the top and bottom surfaces of the tubing directly at the center of each ferrule by pressing down perpendicular to the length of the tubing from either

side. The indented circular holes in the tubing were pulled out with a pair of fine tweezers. Two holes were cut into the silicone to expose the ferrule to allow for better contact while preserving the tubing's mechanical integrity. Any residual silicone oil at the access holes was cleaned off with a Kimtech wipe and Isopropyl Alcohol (IPA).

The two-part silver epoxy was then mixed in a 1:1 ratio and applied to one access hole at a time with a syringe and a 19 AWG needle tip. The epoxy was allowed to contact the inner electrode surface through the access hole and slightly overfilled to form a slight dome. This was then flattened into a $\sim$ 0.1 mm layer by rolling the tubing while applying some pressure (see Figure 2.1 E-F). Since the silver epoxy served both as an electrical and mechanical contact, having an excess amount allowed us to create a strong mechanical bond with the outer electrode without having to glue down the ends, which could have led to kinking and potentially increasing the overall diameter of the electrode line.

The prepared 14 AWG copper ferrule segment was then threaded on top of the tubing until it overlaid the excess epoxy and centers of both the inner and outer ferrules were aligned (see Figure 2.1 G). During this process, a thin wire connected to one probe of a multimeter was threaded through the lumen of the tubing to contact the inner ferrule, and the other probe was made to contact the outer ferrule and resistance was measured continuously to ensure that a good electrical connection was made. Excess epoxy was removed with a Q-tip soaked in IPA. This process was then repeated along the length of the tubing for each electrode. The electrode line was then cured in an oven at 65°C for 2 hours to allow the epoxy to set and form a robust electro-mechanical connection. The full electrode line can be viewed in Figure A.1.

2.3 Sliding Wire Integration

Following electrode curing, two polytetrafluoroethylene (PTFE)-coated stainless steel wires were stripped and ends were bent at 45° angles on one side for both wires. These served as movable contact probes that could slide along the tubing and press against internal electrodes. Bending the ends ensured better contact as the diameter of the wires (0.254 mm) was much smaller compared to the inner diameter of the tubing.

The wires were then offset from each other by the same inter-electrode distance

(reconfigurable for different mapping resolutions) and secured using acrylic glue applied just before the stripped end. Acrylic glue was used since it showed more adhesion to PTFE than cyanoacrylate glues. Each wire acted as a lead for bipolar impedance measurement, allowing rapid scanning without the need for individual wiring of each electrode.

2.4 Calibration

Each electrode was tested for continuity using a multimeter. Resistance between the silver epoxy contact and the internal ferrule was confirmed to be low (< 10 Ω). Neighboring electrodes were also checked for unintended short circuits. The inner-to-outer electrode resistance of each electrode measured at this time (can be found in A.2) was used for calibration of the device during actual testing, summed with the resistances of the wires ($\sim 11\Omega$).

Parameter	**Value**
Inter-electrode spacing (center-to-center)	1 cm
Tubing length	55 cm
Number of electrodes	50
Inner electrode (22AWG) dimensions	ID: 1 mm, OD: 1.3 mm, L: 6mm
Outer electrode (14AWG) dimensions	ID: 2.1 mm, OD: 2.6 mm, L: 6mm
Conductive epoxy thickness	$\sim$0.1 mm
Sliding contact probe dimensions	OD: 0.254 mm, L: 70 cm

Table 2.2: *Design parameters and values.*

2.5 Design Considerations

The fabrication strategy developed for this project was guided by the need for a low-cost, easily manufacturable, and mechanically flexible electrode array capable

of supporting distributed impedance measurements along complex and potentially curved surfaces. To this end, design choices prioritized accessibility of materials and reproducibility over ideal material properties or biocompatibility, making the system particularly well-suited for benchtop prototyping and phantom-based testing.

The choice of silicone tubing with a 1 mm inner diameter (ID) and 2 mm outer diameter (OD) provided a good balance between structural integrity and flexibility. The internal lumen needed to be large enough to accommodate ferrule insertion and allow the sliding wires to pass through without excessive friction, yet narrow enough to ensure that contact was maintained under elastic compression. The tubing was soft enough to deform and conform to non-planar surfaces but not so soft that it collapsed during ferrule insertion or wire threading.

Ferrule dimensions (6 mm in length) and spacing (1 cm center-to-center) were chosen based on preliminary mechanical and electrical trials. Shorter ferrules were found to exhibit higher contact resistance, likely due to poor overlap with the sliding wire probes, while longer ferrules introduced unnecessary stiffness and mass. Spacing under 1 cm was avoided due to the risk of mechanical overlap and increased parasitic coupling between neighboring electrodes.

The decision to insert ferrules via lubrication and mechanical plunging rather than molding them into the silicone was motivated by simplicity and scalability. While this manual insertion method introduced variability in exact positioning and alignment, it enabled fast iteration without custom molds. A tight press-fit, aided by silicone oil, ensured stability of each ferrule along the tubing axis.

Creating dual access holes on either side of the tubing allowed for improved electrical contact and mechanical bonding. Filling both sides with silver epoxy ensured a more robust connection between the inner ferrule and the outer ferrule. Flattening the excess epoxy with controlled rolling prevented radial bulging of the tubing while improving the contact interface area for the outer ferrule.

The sliding-wire configuration was a critical feature enabling reconfigurability and spatial scanning without wiring each electrode individually. Based on preliminary mechanical analysis, it was determined that using thicker wires as contact probes would lead to contact forces which might be unsuitable for use in cardiac applications. However, the small diameter of the Teflon-coated stainless-steel wires relative to the tubing ID introduced contact instability. This was mitigated by bending the ends of

the wires at 45° angles to promote consistent mechanical contact against the ferrule surfaces. Still, occasional variability in contact resistance was observed, particularly if the tubing was compressed or if the wires were loosely guided.

2.6 Design Limitations

A major limitation of the current design was the use of copper as the electrode material. Copper is attractive from a prototyping standpoint due to its affordability, ease of machining, and high conductivity. However, it is chemically reactive in biological or saline environments and prone to oxidation and corrosion. This can lead to time-varying impedance characteristics, reduced signal fidelity, and the formation of passivation layers that affect double-layer capacitance.

For long-term or in vivo applications, a more inert and biocompatible metal such as gold or platinum would be preferable. Gold, in particular, offers excellent corrosion resistance, high conductivity, and mechanical softness, which improves contact compliance. It is also commonly used in biomedical electrode arrays and would be a direct drop-in replacement in the existing fabrication pipeline. However, cost and machining difficulty present practical barriers for early-stage prototyping. As such, the current copper-based configuration should be viewed as a proof-of-concept platform, with the expectation of material upgrades for clinical or production use.

While the entire fabrication protocol was designed for benchtop reproducibility, several manual steps introduced variability between batches. These include the precision of inter-electrode spacing, access hole alignment, and the volume and placement of silver epoxy. In addition, the silver epoxy's consistency and working time had a significant effect on bonding quality. In future versions, the use of jigs or fixtures to standardize ferrule positioning, hole cutting, and epoxy application could improve consistency and throughput.

The final electrode line retained a slim profile ($\sim$2.6 mm diameter), allowing it to be easily embedded in grooves or phantom tissues. However, the double-ferrule design increased the radial footprint compared to designs that use embedded traces or surface electrodes. For applications requiring extreme miniaturization or multi-layer integration, further reductions in outer ferrule height or alternative fabrication methods (e.g., embedded mesh, conductive elastomer molding) may be warranted.

Chapter 3

Experimental Design and Setup

3.1 Phantom Fabrication

To evaluate the performance of the soft electrode array under realistic deployment conditions, a series of tissue-mimicking phantom substrates were fabricated using agar-based gels. Agar was chosen due to its controllable mechanical properties, ease of molding, and wide usage in bioelectrical research. The formulation and post-processing steps closely followed protocols validated by Kandadai et al. [12], with modifications to accommodate electrode insertion and complex surface geometries. This chapter outlines the materials, fabrication procedures, and mold designs used to create four distinct phantom geometries for evaluating sensor conformity and impedance behavior. Table 3.1 summarizes the materials and equipment used for fabricating the phantoms. Figure 3.1 shows the fabricated phantoms for EIS testing and a ventricular model for mechanical validation.

3.1.1 Gel Preparation

Agar phantom gels were prepared using a standardized formulation of 1.5 g agar powder and 1.0 g sodium chloride dissolved in 100 mL of deionized water. This composition yielded a gel with sufficient mechanical stiffness to simulate soft tissue deformation under mild loading while maintaining ionic conductivity suitable for impedance spectroscopy.

Material/Equipment	**Vendor**	**Purpose**
Agar Powder	Yuantide Bio-tech	Gel matrix
Sodium Chloride (NaCl)	Sigma-Aldrich	To provide ionic conductivity
Deionized (DI) water	Sigma-Aldrich	Solvent for gel preparation
SolidWorks 3D CAD Software	Dassault Systèmes	Mold design
FormLabs 3B+ Printer	FormLabs	3D printing of molds
Tough 2000 Resin	FormLabs	High strength mold material
Glass Beaker	Generic Supplier	Gel preparation
Hotplate with Magnetic Stirrer	Scilogex	Heating and mixing agar solution
Mineral Oil	Vaseline	Optional – to ease phantom demolding
Fine-tip spatula or tweezers	Generic Supplier	Phantom handling and removal
Refrigerator	Generic Supplier	Phantom curing and storage

Table 3.1: *Materials and equipment used in the fabrication of agar phantoms.*

The DI water was first heated to ∼90°C using a hotplate with magnetic stirring. Once the water reached temperature, sodium chloride (NaCl) was added and dissolved fully, followed by gradual addition of agar powder while stirring continuously to avoid clumping. The solution was maintained near boiling (∼95°C) for an additional 10–15 minutes until the agar had completely dissolved and a homogeneous solution was obtained.

After the solution was clarified and no visible particulates remained, it was removed from heat and allowed to cool slightly (to ∼70°C) before pouring into pre-cleaned and leveled molds. This temperature range prevented deformation of the 3D printed mold while still ensuring fluidity for accurate casting.

3.1.2 Mold Design and Fabrication

Each mold was custom-designed in SolidWorks 2024 based on the geometry of interest. Designs incorporated shallow grooves or channels on the mold floor to constrain and stabilize the electrode line during testing. The CAD models can be viewed in A.3. Molds were printed using the FormLabs 3B+ SLA printer with Tough 2000 resin, chosen for its dimensional stability and surface smoothness. Post-processing included IPA washing, air drying, and post-curing under UV light according to manufacturer specifications. A thin layer of mineral oil was applied to facilitate demolding of the cured agar phantom. The dimensions of the cylindrical molds were informed by the results of the mechanical analysis covered in Section Chapter 4.

For the cylindrical phantom, a three-part mold was employed. This design included two radially split cylindrical halves and a central insert with a handle for easy removal. When assembled, the mold allowed vertical pouring and produced a clean circular cross section.

3.1.3 Phantom Geometry Overview

Four distinct phantom geometries were used to test the sensor's electrical performance under diverse curvature and surface conformity conditions:

1. *Flat Straight Phantom (Control)*
   A rectangular phantom block with a shallow linear groove along the top surface (see Figure 3.1 A). This geometry was used to establish baseline measurements under minimal curvature or contact complexity, providing a reference for performance under ideal conditions.
2. *Flat Loop Phantom*
   A variation of the flat phantom featuring a circular (loop) groove along the top surface (radius = 2 cm) (see Figure 3.1 B). This design introduced localized surface undulations to simulate mild but distributed curvature, testing how the sensor responded to non-uniform, planar surface variation.
3. *Convex Cylindrical Phantom*
   A cylindrical phantom over which the electrode line was wrapped externally in a helical pattern, used to evaluate performance under continuous outward

curvature and wrapping (radius = 3 cm) (see Figure 3.1 C). This setup simulated deployment on convex anatomical surfaces such as the outer wall of a blood vessel, gastrointestinal tract, or limb. The consistent outward curvature provided a testbed for evaluating sensor adherence and electrical performance on large-radius curved surfaces.

4. *Concave Cylindrical Phantom*
   A cylindrical phantom with a hollowed-out inner cavity (radius = 2 cm) (see Figure 3.1 D). The electrode was wrapped inside this cavity, conforming to the inner wall without the aid of a guiding groove. This tested the sensor's ability to maintain contact in recessed or negative curvature environments, such as cardiac chambers, or deep tissue creases. The mold used to cast this geometry featured a cylindrical core insert with a handle to facilitate demolding.

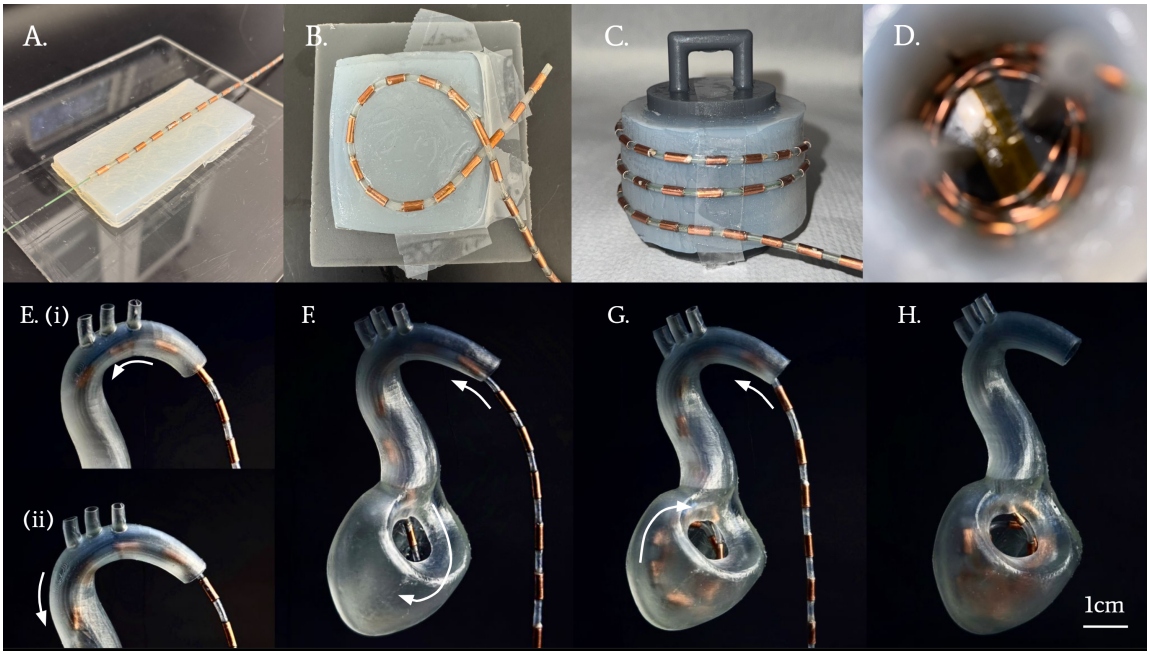

Figure 3.1: *Fabricated phantoms for testing.*
A. Straight line configuration. **B.** Single loop configuration. **C.** Convex (outside cylinder) configuration. **D.** Concave (inside cylinder) configuration. **(E - H):** Mechanical demonstration of soft electrode line deployment through a physiologically representative aortic and left ventricular model.

Additionally, another phantom (Figure A.4) was made for a flat angular curvature test performed to evaluate impedance behavior across varying degrees of in-plane curvatures (0° - 90°, in 15° increments). This was done by adding additional grooves to the phantom at specific angles.

All phantoms were cast with the same agar formulation and cured for at least 2 hours in a refrigerator before use. Prior to testing, phantoms were allowed to equilibrate to room temperature for 30 minutes.

3.2 Preliminary Mechanical Testing with Ventricle Model

To evaluate the mechanical adaptability of the electrode line in a physiologically relevant setting, I first performed a deployment test using a 3D-printed model of the human aorta and left ventricle (printed with FormLabs Clear Resin). This model featured realistic anatomical curvature and chamber topology, offering a more complex substrate than the simplified agar phantoms, although it was non-conductive. The electrode line was manually guided through the aortic inlet and allowed to settle along the inner ventricular wall under its own flexibility, without external fastening or adhesives. As shown in Figure 3.1 (E–H), the device was able to navigate sharp bends and settle into contact with the inner surfaces of the model, demonstrating its conformability to highly folded or recessed biological geometries. This test served as a qualitative mechanical verification that the sensor's stiffness and form factor were compatible with endocardial-scale deployment scenarios, supporting its relevance to anatomically embedded sensing applications.

3.3 Experimental Setup for Electrical Impedance Spectroscopy (EIS)

To evaluate the electrical performance of the fabricated soft electrode array under varied geometrical and loading conditions, impedance measurements were conducted using electrical impedance spectroscopy (EIS). All measurements were performed

using a benchtop LCR meter (BK Precision 890 20Hz - 500kHz LCR Meter) configured to operate over a defined frequency range relevant to bioimpedance characterization. This section outlines the measurement protocol, instrumentation settings, phantom mounting strategy, and procedures for sensor connection and data acquisition.

The following parameters were used consistently across all tests unless otherwise specified:

- Frequency range: 1 kHz to 100 kHz (linearly spaced over 200 measurements)
- Voltage excitation amplitude: 1V peak-to-peak (AC signal)
- Measurement mode: Z–d (Impedance magnitude and phase (degrees))
- Terminal configuration: Two-terminal bipolar mode
- Integration time: Medium (balanced for noise and speed)

All measurements were logged using the instrument's software interface and exported as raw CSV files for subsequent analysis and curve fitting using Python.

Each impedance test was performed with the electrode line embedded into one of four predefined phantom geometries, fabricated from NaCl–agar gel. All measurements were conducted in air, without the use of saline or additional conductive media. The electrode–phantom contact was established through passive conformity and gentle placement, mimicking realistic contact scenarios for dry or semi-dry surface measurements. For each geometry, visual inspection was used to ensure that the gel was intact and the electrode was flush against the phantom surface.

Impedance measurements were conducted using the two PTFE-coated stainless steel sliding wires integrated into the electrode tubing. These wires served as dynamic bipolar probes and were aligned manually with the desired copper electrodes along the electrode line.

The spacing between the wires was adjusted according to the inter-electrode distance of the device. Alignment was guided by the external electrode positions and verified via multimeter to ensure electrical continuity. Resistance across each contact was expected to be within calibration limits; values exceeding this threshold prompted realignment or re-contacting. Each wire was connected to the LCR meter using alligator leads. Care was taken to prevent lead movement during measurements and to avoid contact with the gel itself.

For each phantom geometry, three full trials were performed. Each trial used a

freshly fabricated phantom block and independently re-placed electrode line. Within a single trial, the sliding wires were repositioned to measure across multiple electrode pairs ($\sim$ 30), covering various inter-electrode distances and contact regions, and the average response for a trial was used to compute a representative impedance spectrum for each geometry. Contact quality was confirmed before logging data for each geometry.

To evaluate impedance response with different loading conditions (contact pressures) for the straight line geometry, a plastic (insulated) petri dish was placed on top of the electrode line to which weights were added in 20 g increments (up to 160 g). Measurements were taken at discrete frequencies to evaluate behaviour across the frequency spectrum. To evaluate impedance response at different 2D angular curvatures, the same setup was used with a fixed weight of 40g added to reduce influence of contact pressure due to curvature.

Chapter 4

Results & Discussion: Mechanical Performance

4.1 Material Stiffness and Contact Force

The ability of the electrode line to conform to curved anatomical structures is governed by the interplay between its internal stiffness and the curvatures imposed by the environment. Exceeding contact force limits for particular types of tissue can result in perforations and damage. In the case of an embedded system composed of soft tubing, discrete rigid electrodes, and an internal wire, understanding which component dominates the mechanical response is critical for assessing deployment performance, tissue safety, and passive versus active navigation strategies.

The mechanical analysis conducted in this study relied on several simplifying assumptions to enable tractable, first-order approximations of stiffness and contact force. The electrode line was modeled as a composite beam consisting of alternating soft tubing and rigid (or semi-rigid) electrode segments, with mechanical behavior governed by Euler-Bernoulli beam theory under quasistatic, small-deformation conditions. The stainless steel wires threaded through the tubing were assumed to have uniform stiffness and span the entire length of the array without slippage. For contact force estimation, the bent sensor was idealized as a circular arc, with moment–curvature relationships used to derive tip contact forces. Tissue was modeled

as rigid and non-compliant, with no distributed contact or frictional effects considered. These assumptions, while conservative, allowed us to identify key stiffness bottlenecks and establish upper bounds on safe bending curvatures and expected forces for physiological use.

We first analyze which component — the internal wire or the external tubing-electrode structure — primarily dictates the bending resistance of the device. This is done by calculating the flexural rigidity of each component, a measure of a structure's resistance to bending. A higher flexural rigidity indicates a stiffer element under bending loads. The embedded wire is a 0.254 mm diameter wire made with stainless steel 304 of spring temper. For this analysis, I consider one electrode line segment to comprise one tubing element of length 4mm and one electrode element of length 6mm. Because these regions are in series along the length of the electrode line and experience the same bending moment, their combined angular deflections can be summed to compute the total deflection for a 10 mm structural segment. Material property summaries used for this analysis can be found in Table 4.1.

	Tubing	**Electrode**	**Wire**
Material	Silicone	Copper	Spring Temper 304SS
Young's Modulus	1 MPa	110 GPa	200 GPa
Dimensions	ID: 1 mm, OD: 2 mm, L = 4mm	ID: 1 mm, OD: 2.6 mm, L = 6mm	OD: 0.254 mm, L = 10mm

Table 4.1: *Material properties and dimensions for tubing, electrode, and wire.*

The resistance to bending of a structure is characterized by its flexural rigidity (D), given by:

$$D = EI \tag{4.1}$$

where E is the Young's Modulus of the material and I is the second moment of area of the cross-section.

For a cylindrical structure such as a tube or a wire of diameter d, I can be calculated as:

- **For a solid cylinder (such as a wire)**

$$I = \frac{\pi}{64} d^4 \tag{4.2}$$

- **For a hollow cylinder (such as a tube)**

$$I = \frac{\pi}{64} (d_{outer}^4 - d_{inner}^4) \tag{4.3}$$

Once D is known, the moment M required to achieve a curvature $\kappa = \frac{1}{R}$ (where R is the bending radius) is given by:

$$M = D\kappa \tag{4.4}$$

For each segment, total angular deflection under moment M is the sum of the deflections in the electrode and the tubing:

$$\theta_{seg} = \theta_{electrode} + \theta_{tube} \tag{4.5}$$

$$= \frac{L_{electrode}}{R_{electrode}} + \frac{L_{tube}}{R_{tube}} \tag{4.6}$$

$$= \kappa_{electrode} L_{electrode} + \kappa_{tube} L_{tube} \tag{4.7}$$

$$= \frac{M L_{electrode}}{D_{electrode}} + \frac{M L_{tube}}{D_{tube}} \tag{4.8}$$

We define the equivalent segment stiffness $D_{segment}$ as:

$$D_{segment} = \frac{M}{\kappa} = \frac{M L_{segment}}{\theta_{segment}} \tag{4.9}$$

From Equations 4.8 and 4.9,

$$\frac{L_{segment}}{D_{segment}} = \frac{L_{electrode}}{D_{electrode}} + \frac{L_{tube}}{D_{tube}} \tag{4.10}$$

$$\implies D_{segment} = \frac{L_{segment}}{\frac{L_{electrode}}{D_{electrode}} + \frac{L_{tube}}{D_{tube}}} \tag{4.11}$$

Equation 4.11 allows us to compute an effective flexural rigidity for the heterogenous

segment by combining stiffness contributions from both components based on their lengths and materials. Hence,

$$I_{wire} = 2.04 \times 10^{-16} m^4$$
$$I_{electrode} = 2.06 \times 10^{-12} m^4$$
$$I_{tube} = 7.36 \times 10^{-14} m^4$$

Using the harmonic mean formulation for a composite segment (electrode + tube) and material properties listed in Table 4.1,

$$D_{wire} = 4.09 \times 10^{-5} N \cdot m^2$$
$$D_{segment} = 1.84 \times 10^{-6} N \cdot m^2$$

To evaluate the impact of multiple conductors, I consider the two-wire configuration. Consequently, the effective stiffness of a two-wire configuration will be between that of a single wire and exactly double, depending on the degree of coupling. For conservative curvature estimates, it is reasonable to treat the combined stiffness as close to $2D_{wire}$ (i.e., a doubling of the bending moment required to achieve the same curvature). This assumption ensures that safety margins for force limits are not underestimated.

$$D_{2-wires} = 8.18 \times 10^{-5} N \cdot m^2$$

This results in a stiffness ratio > 44, i.e. the wire is over 44 times stiffer in bending than the composite segment. As a result, even if the surrounding structure is relatively soft, the wire alone limits the achievable curvature and dominates the mechanical behavior of the electrode line.

The contact force exerted by a bent electrode line on surrounding tissue is modeled as a distributed reaction. Following a strain-energy approach for an elastic beam bent into a circular arc of radius ρ, the strain energy per unit length is

$$u = \frac{M^2}{2EI}, \tag{4.12}$$

where M is the bending moment and EI is the flexural rigidity. For a full loop of

radius ρ, the total stored energy is

$$U = \int_0^{2\pi\rho} \frac{M^2}{2EI}\, dl = \int_0^{2\pi\rho} \frac{EI}{2\rho^2}\, dl = \frac{\pi EI}{\rho}. \tag{4.13}$$

If the loop tightens from radius ρ to $\rho - \Delta\rho$, the incremental work done by the distributed radial reaction q is

$$\Delta W = \Delta\rho \int_0^{2\pi\rho} q\, dl = 2\pi\rho q \Delta\rho, \tag{4.14}$$

and the corresponding increase in potential energy is

$$\Delta U = \frac{dU}{d\rho}(-\Delta\rho) = \frac{\pi EI}{\rho^2}\Delta\rho. \tag{4.15}$$

Equating $\Delta W = \Delta U$ and solving for q gives the distributed contact force per unit length:

$$q = \frac{EI}{2\rho^3}. \tag{4.16}$$

For the two-wire probe, the stiffness is dominated by the two stainless-steel conductors such that $EI \approx 2D_{\text{wire}}$. Substituting this into the expression simplifies to

$$q_{\text{wires}} = \frac{D_{\text{wire}}}{\rho^3}. \tag{4.17}$$

The distributed force on a segment of length L_{segment} is then

$$F_{\text{segment}} = q\, L_{\text{segment}}. \tag{4.18}$$

Using $L_{\text{segment}} = 10$ mm $= 0.01$ m, the distributed contact forces are computed for several bend radii as summarized in Table 4.2.

This helps identify the same limits of achievable curvature without exceeding physiological thresholds. Clinical literature suggests that contact forces exceeding 40 g (approximately 0.4 N) [27] may pose risks of endocardial damage or adverse mechanical interaction with tissue.

Bend Radius $\mathcal{R}$ (mm)	**Curvature κ (1/m)**	q_{wires} **(N/m)**	q_{segment} **(N/m)**	F_{wires} **(N)**	F_{segment} **(N)**
50	20	0.327	0.00736	0.00327	0.0000736
20	50	5.11	0.115	0.0511	0.00115
10	**100**	**40.9**	0.921	**0.409**	0.00921
5	200	327.2	7.37	3.27	0.0737

Table 4.2: *Distributed contact force estimates for a 10 mm segment. Both the stiff two-wire configuration and the compliant tubing-electrode segment are shown.*

These findings have important implications for the design and deployment of the electrode line. While the tubing-electrode segment itself remains highly compliant, generating less than 0.07 N of contact force even at the tightest bend radius considered, the embedded stainless steel wires substantially increases the total stiffness of the system. From Table 4.2, a force threshold of 0.4 N is exceeded by the embedded wire at bend radii smaller than approximately 1 cm. Thus, under passive deformation, the minimum safe curvature that can be achieved without exceeding this physiological contact force limit is around 1 cm.

4.2 Plastic Deformation of Wire

Another potential failure mode of the electrode line arises from the risk of plastic deformation in the internal stainless steel wires, since exceeding the material's yield point would result in permanent mechanical damage and altered deployment behavior. This is especially relevant in dynamic or constrained environments where sharp curvatures may be imposed during navigation or operation.

In this context, the yield threshold of the wire becomes a critical mechanical limit. Spring-tempered variants of stainless steel are significantly stiffer than annealed wire, with yield strengths typically ranging between 1200–1500 MPa. To maintain a conservative estimate while ensuring safety margin, I assume a lower bound yield strength of $\sigma_y = 1200$ MPa.

To determine the curvature at which plastic deformation begins, I use the standard

formula for maximum bending stress in a circular wire:

$$\sigma_{max} = E \cdot \kappa \cdot \frac{d}{2} \tag{4.19}$$

Setting $\sigma_{max} = \sigma_y$,

$$\kappa_{yield} = \frac{2\sigma_y}{Ed} \approx 47.24m^{-1} \tag{4.20}$$

This corresponds to a minimum bend radius of 21.2 mm.

While contact force considerations provide one important constraint, these calculations show that plastic deformation becomes the more stringent limiting factor: at a bend radius of approximately 2 cm, the maximum bending stress reaches the material's yield strength. Beyond this point, the internal conductors are no longer guaranteed to remain in their elastic regime, and permanent damage such as work-hardening or microcracking may occur. The 2 cm bend radius therefore becomes the defining minimum radius of curvature for this design. Any sharper bend — whether due to overshoot during deployment or navigation through tortuous anatomy — risks irreversible damage to the wire, potentially compromising long-term durability and deployment repeatability.

These findings define a practical design constraint: while the current wire-based architecture is sufficient for moderate curvature and stable deployment, it may not be suitable for applications requiring passive conformity to highly curved or tortuous anatomy. In such cases, redesigning the internal conductor with more compliant materials—such as superelastic nitinol, liquid-metal-filled elastomers, or conductive silicone composites—could significantly improve the safe bending range. Moreover, future versions of the electrode line may benefit from stiffness-tunable materials that change mechanical properties dynamically. Thermoresponsive or magnetoactive polymers, for instance, could enable low-stiffness insertion followed by structural reinforcement once in place, striking a balance between conformity and support. These approaches would expand the adaptability of the system and reduce the risk of material fatigue in demanding geometries.

This preliminary mechanical analysis directly informed the curvature limits selected during phantom fabrication for experimental testing. Specifically, the identification of a $\sim$2 cm minimum safe bend radius—based on the yield point of the internal

spring-temper stainless steel wires—guided the design of the most extreme concave test geometry. By using this analytically determined radius as the lower bound, I ensured that the electrode line would operate within its elastic regime while still being challenged by anatomically relevant curvature. This deliberate constraint enabled us to isolate mechanical confounds during testing and focus on the electrode line's electrical performance under controlled but realistic deformation.

4.3 Mechanical Robustness of the Epoxy–Tubing Interface

The electrical and mechanical reliability of the electrode array critically depends on the integrity of the bond between the silver epoxy and the surrounding silicone tubing. This bond anchors the outer copper ferrule to the device body and provides electrical continuity between the sliding wire and the outer electrode. Mechanical failure at this interface could compromise signal conduction or even cause ferrule detachment under bending. The detailed methodology and results from the FEA study are provided in Section A.4.

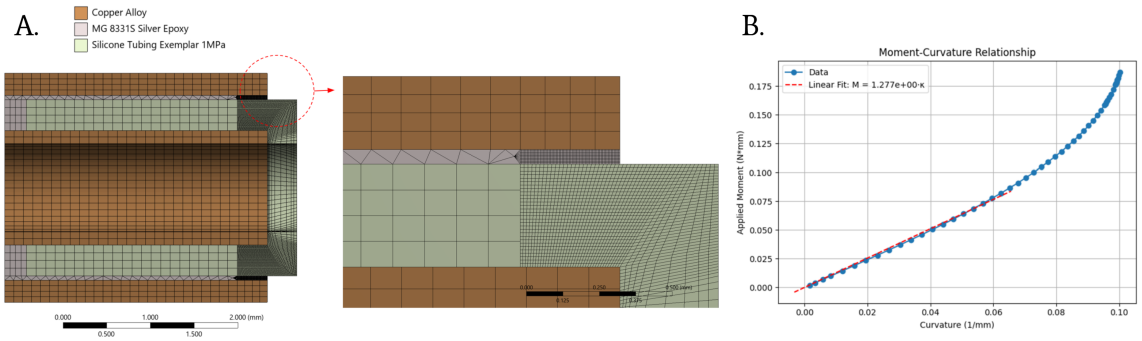

Figure 4.1: *Finite-element analysis (FEA).*
A. Mesh setup. **B.** Bending moment vs. Curvature relationship.

To assess this risk, I conducted a finite element analysis (FEA) in collaboration with Dr. David Quinn. The study modeled a representative electrode–tubing–epoxy segment under physiological bending conditions, using isotropic linear elastic material properties and realistic dimensions. A bending moment was applied at one end of the

structure to simulate deformation into a 2 cm radius - consistent with the expected minimum deployment curvature.

Relevant Failure Mode	**Max Value**	**Critical Value**	**Failure a Concern**
Max elongation of epoxy material	0.19%	5.30%	No
Max elongation of tubing material	34.05%	700%	No
Interfacial/bond failure: Epoxy / Tubing Interface	1.7645 MPa	0.1 MPa*	**Yes**
Interfacial/bond failure: Epoxy / Outer Electrode Interface	0.2795 MPa	1 MPa**	No
Failure Strength of epoxy material	2.0072 MPa	13.8 MPa	No
Failure Strength of tubing material	0.34952 MPa	1 MPa – 10 MPa	No

Table 4.3: *Comparison of maximum stress or strain values to material or interfacial limits for each failure mode.*
*Estimate lap shear strength between epoxy and silicone as an order of magnitude less than spec sheet values for Aluminum and Stainless Steel.
**Estimate lap shear strength between epoxy and copper electrode to be comparable to spec sheet value for epoxy with Stainless Steel.

The FEA results revealed that the dominant failure mode is interfacial shear at the epoxy–tubing interface (as summarized in Table 4.3), particularly at the uppermost tensile edge where peeling stresses are concentrated. The interfacial shear stress exceeded estimated bond strength ($\sim$0.1 MPa) in a narrow region ($<$0.5 mm) along the outer edge of the bond. However, the remainder of the bonded region remained well below critical thresholds, and no delamination was observed across the central or lower compressive zones.

Despite localized bond stress, the electromechanical integrity of the system is unlikely to be compromised unless the entire outer ferrule detaches - an event not predicted by FEA. Electrical continuity is maintained through centrally located access holes that provide a short, low-resistance path from the inner sliding wire to the outer

electrode. These access points were not explicitly modeled in the FEA, meaning the results represent a conservative overestimate of potential failure. Additionally, the stress concentration will likely not be this severe since the FEA modeled the epoxy edge as a sharp corner. In reality there will be some taper that might help reduce the stresses.

Mechanically, the system is further stabilized by the over-constrained ferrule geometry. Because the electrode line bends symmetrically during insertion, peak stresses are distributed rather than localized to one side. This further reduces the risk of progressive crack propagation or gross delamination. Electrically, we device might see a slight change in parasitic capacitance due to the formation of small air gaps at the delaminated edge, but this is expected to be marginal and wouldn't influence near-term impedance measurements.

While these results suggest that short-term functionality is robust under deployment-level bending, the FEA does highlight potential long-term reliability concerns. Repeated flexing or moisture ingress could degrade adhesion at the epoxy–tubing boundary over time. Future work could incorporate accelerated aging tests or direct shear measurements to validate bond durability.

In summary, the FEA supports the conclusion that while localized interfacial delamination may occur, the overall electromechanical performance remains intact during deployment. These findings validate the epoxy–tubing interface design for the current proof-of-concept system.

4.4 Limitations

While this study provides a first-order mechanical characterization of the electrode line, several limitations constrain both the generalizability of the results and the robustness of the design in physiological contexts.

First, the mechanical analysis was conducted entirely analytically, with no experimental validation of flexural rigidity, curvature response, or contact force. Key assumptions—such as quasistatic loading, perfect bonding between components, and a rigid, non-compliant tissue substrate—neglect real-world effects like viscoelastic damping, tissue deformation, and slippage between the wire and surrounding elastomer. Furthermore, only planar bending was considered; torsional loads, shear-induced mo-

tion, and dynamic actuation were not modeled, despite their relevance in navigating tortuous anatomical pathways.

From a design standpoint, the dominant mechanical limitation arises from the embedded stainless steel wire. This internal component sets the effective lower bound on bend radius to approximately 20 mm—due to the plastic deformation thresholds of spring-temper stainless steel wires. As a result, the device may be too stiff to conform passively to highly curved anatomical regions without risk of mechanical failure.

Fabrication-related factors further limit mechanical performance. Manual insertion of the wire into soft tubing increases the risk of residual curvature and inconsistent straightness, which can pre-bias the deployed shape. Misalignment between tubing and electrodes during assembly introduces local stress concentrations and may impair uniform bending. Moreover, the lack of strain relief or mechanical decoupling near connections could create failure points during cyclic loading or sharp navigation maneuvers.

In total, the current prototype is well-suited for moderate-curvature applications and structured phantom testing, but would require significant redesign—such as softer conductors, mechanically decoupled segments, or alternative composite layering strategies—to ensure safe and robust deployment in soft, dynamic, or highly curved biological environments. Experimental testing and durability studies will be critical next steps to validate and extend these findings beyond the constraints of this initial analysis.

Chapter 5

Results & Discussion: Electrical Performance

The experimental setups for the EIS tests are given in Figure 5.1.

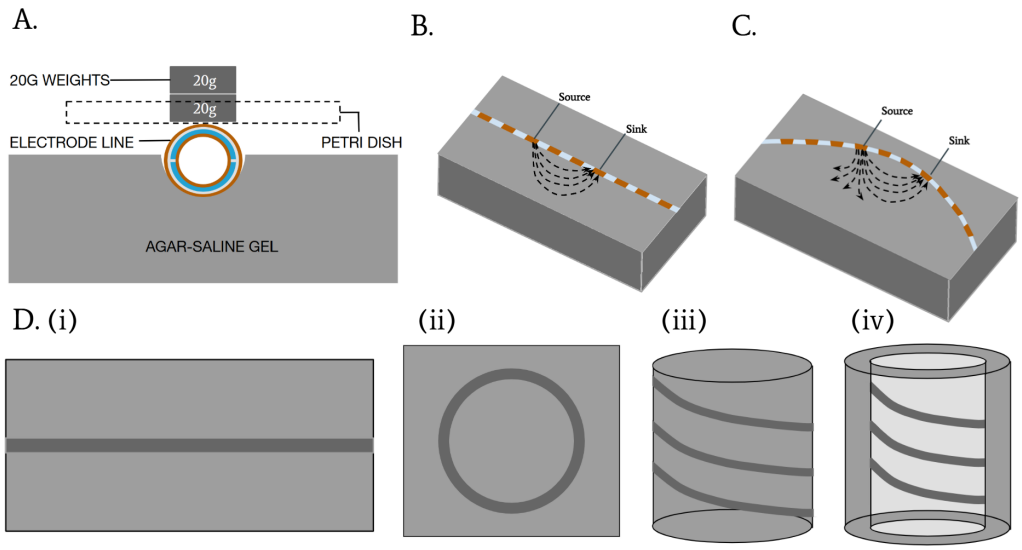

Figure 5.1: *Experimental setup for testing.*
A. Electrode line lying in a groove in straight line configuration with weights added. **B.** Electrode line in straight line configuration with field lines. **C.** Electrode line in curved configuration with field lines. **D.** Geometries for testing: **(i)** Straight line **(ii)** Single Loop **(iii)** Convex **(iv)** Concave.

5.1 Impedance Trends with Added Weight (Straight Configuration)

In the flat, straight configuration, adding normal load (weights) on the soft copper electrode line produced a clear and monotonic decrease in impedance magnitude across the frequency spectrum as seen in Figure 5.2. As weight increased, the electrode was pressed more firmly into the electrolyte or tissue, improving contact and reducing interfacial resistance. This effect was especially pronounced at low-mid frequencies (e.g., 20 kHz), where the impedance magnitude decreased substantially with added weight—indicating a drop in polarization resistance and enhanced charge transfer due to improved mechanical contact.

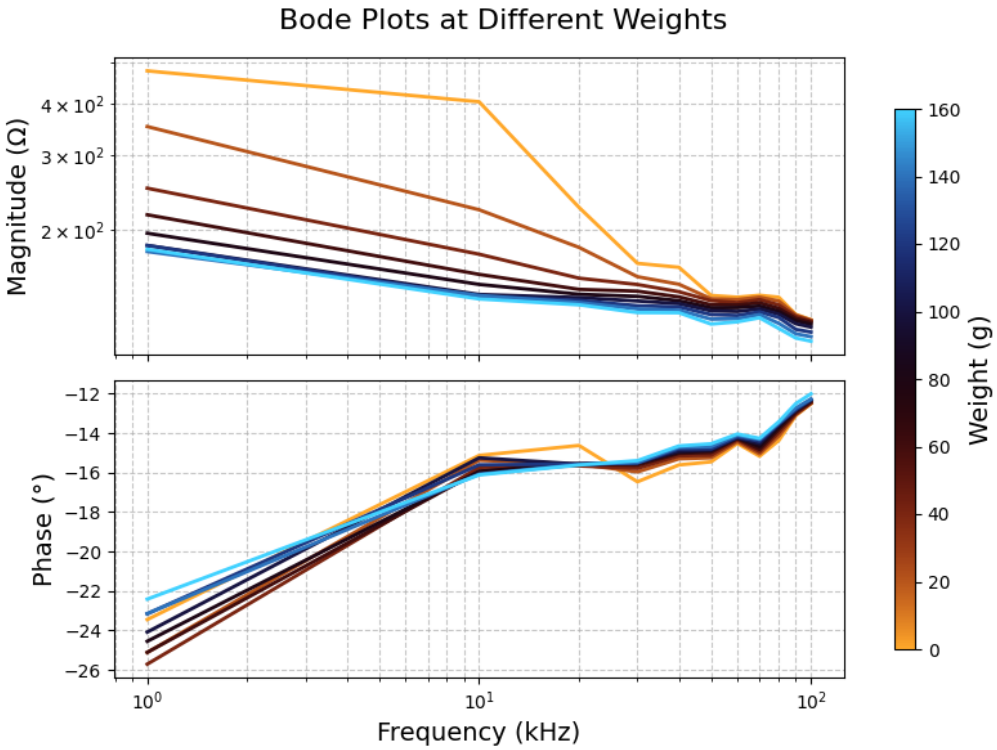

Figure 5.2: *Impedance response with addition of weights (contact pressure) for straight line geometry.*

At higher frequencies, the impedance magnitude remained relatively stable, consistent with expectations that solution resistance and wiring dominate in this regime

and were less influenced by physical pressure. In contrast, the phase response showed minimal variation across loading conditions. While there was a slight trend of low-frequency phase becoming less negative (closer to 0°) at heavier loads, the overall change was subtle and not monotonic. Similarly, in the mid-frequency range, phase angles remained largely constant, suggesting that the double-layer capacitance and distributed time constants were not significantly altered by applied load in this geometry.

These findings suggest that while added normal load on a flat electrode improves mechanical contact, it does so uniformly across the entire surface, primarily reducing the interfacial resistance without appreciably altering the distribution of current densities or the time constants; hence, the phase remains largely unchanged. However, even when gross contact appears uniform, geometric factors such as curvature might alter the distribution of local current density in ways that simple contact pressure does not.

5.2 Impedance Trends with Increasing In-Plane Curvature (2D Substrate)

To isolate how geometric deformation alone influenced electrical behavior, I investigated impedance changes as a function of angular curvature—from 0° to 90°—on a flat 2D substrate. The electrode was manually bent into increasing in-plane angles while maintaining continuous contact with a homogeneous agar phantom. A consistent normal load was applied during each test to ensure adequate contact. However, even though gross detachment was avoided, local variations in pressure across the inner and outer arcs were unavoidable. Figure 5.3 illustrates the impedance response at different curvature angles. These tests reflect challenges in real-world use cases—such as wrapping around curved organs, threading through narrow anatomical pathways, or integrating with soft robotic devices—where small geometric shifts can cause local detachment or uneven contact, disrupting sensing performance.

The impedance magnitude plot revealed inconsistent variation with curvature, especially at high frequencies (80–100 kHz). This suggested that the impact of curvature on resistive components may not follow a simple linear trend in this

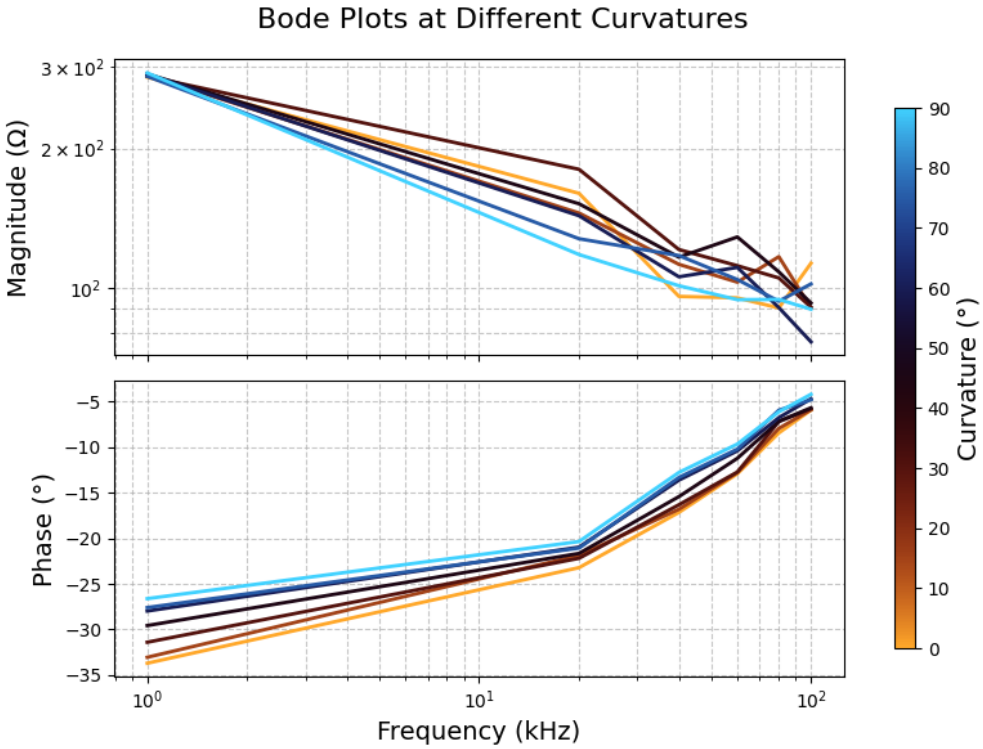

Figure 5.3: *Impedance response with increasing angular curvature in 2D.*

controlled 2D regime. The phase behavior, by contrast, exhibited a clear and consistent trend: as curvature increased, the phase angle became progressively less negative across most of the frequency spectrum. This indicated a transition toward more resistive behavior, with reduced capacitive storage dominating the interface especially at low frequencies. Notably, this resistive shift emerged even though contact conditions were designed to be uniform, implying that geometric distortion alone can substantially alter current distribution and interface dynamics.

One key consideration is how curvature alters local contact pressure. The inner arc of a bent electrode may compress more firmly against the substrate under uniform weight, forming small zones of concentrated current flow, while the outer arc may become partially shielded. This would increase local field gradients and reduce the uniformity of current paths, effectively redistributing the double-layer interface. As a result, even if total contact area remains roughly constant, the asymmetry in current density can suppress capacitive charge storage and compress the effective

time constants of the system.

In addition, geometric curvature may introduce subtle physical deformations at the microinterface: stretching or compression of the electrode-tissue interface could degrade the electrochemical double layer or increase surface heterogeneity. These effects would reduce the capacitive contribution at mid frequencies and accelerate the transition to resistive behavior, as reflected in the less negative phase angles.

Test Condition	**Low f** (1–10 kHz)	**Mid f** (20–60 kHz)	**High f** (80–100 kHz)	**Physical Interpretation**
Increasing Contact Pressure	$\|Z\|$ decreases Phase increases moderately	$\|Z\|$ decreases moderately Phase almost constant	$\|Z\|$ nearly constant Phase almost constant	Improved contact area reduces polarization resistance. Capacitive behavior largely unchanged due to stable double-layer formation.
Increasing Angular Curvature	$\|Z\|$ stable or slightly decreases Phase increases	$\|Z\|$ inconsistent Phase increases moderately	$\|Z\|$ inconsistent Phase nearly 0°	Geometric curvature introduces field distortion and asymmetric current paths, reducing overall capacitive behavior despite maintained contact.

Table 5.1: *Summary of frequency-dependent impedance trends with contact pressure and angular curvature.*

Thus, the contact pressure and 2D curvature tests established a baseline for understanding how simple geometric deformation and contact quality can shift impedance behavior, even under controlled immersion and contact conditions. In the following sections, I extend this analysis to more complex geometries—including single-loop bends, convex arcs, and concave chambers—where additional 3D field interactions and asymmetric wetting further complicate the impedance response.

5.3 Impedance Trends Across Geometries

To evaluate how electrode geometry influenced electrical performance, the electrode line was tested in four configurations: flat straight, flat loop, convex (wrapped around the outside of a cylinder), and concave (embedded inside a cylinder). These configurations represented increasing geometric curvature and varying degrees of mechanical conformity. All measurements were conducted in conductive agar under matched conditions to isolate geometric effects. Impedance trend plots for individual geometries for each trial can be found in Appendix Section A.5. Figure 5.4 illustrates the impedance trends across geometries for 1 trial.

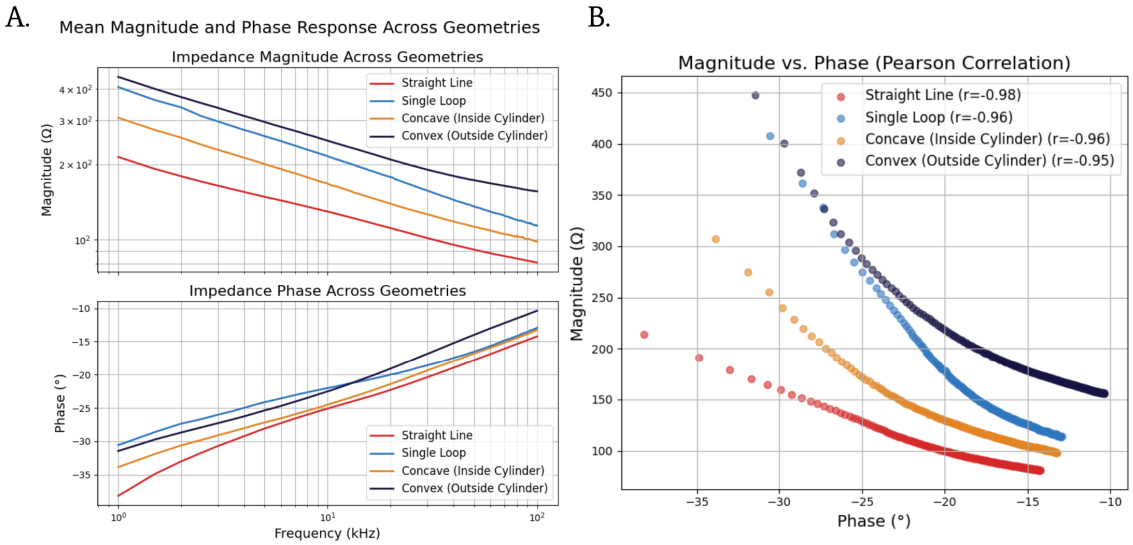

Figure 5.4: *Impedance trends and magnitude-phase correlation across geometries.* **A.** Mean impedance magnitude and phase across frequency for four geometries. Curved geometries show higher impedance and phase shifts. **B.** Strong negative correlation (r ≈ -0.94 to -0.98) between magnitude and phase highlights consistent geometry-dependent effects.

Impedance magnitude demonstrated a consistent geometry-dependent trend. As curvature increased and conformity worsened, overall $|Z|$ values generally rose. The flat straight configuration showed the lowest impedance across all frequencies, while the convex geometry exhibited the highest. The concave configuration—despite having higher curvature—displayed lower impedance than the convex case. This

reversal suggested that inward bending and innate stiffness due to the sliding contact probes may have enhanced real contact by pressing the electrode more uniformly into the gel, whereas convex bending likely lifted parts of the electrode away, disrupting the ionic interface and increasing resistance.

Phase angle behavior further clarified these effects. At high frequencies, all configurations approached 0°, reflecting a resistive regime. In the mid-frequency range (20–60 kHz), capacitive contributions became more pronounced. The flat straight configuration exhibited the most negative phase angles in this band while the convex and single loop geometry showed the least capacitive behavior, with the least negative phase angles. The concave configuration again exhibited intermediate behavior between the flat and convex cases, consistent with the idea that inward bending helps preserve more uniform physical contact. These observations also mirror the results of the 2D angular curvature tests, where introducing curvature tended to shift the response toward more resistive behavior by distorting current paths and altering how charge is distributed across the interface.

Pearson correlation analysis between phase and magnitude supported these trends. The strongest negative correlation ($r \approx -0.98$) was observed in the flat geometry, indicating consistent impedance-phase coupling. As curvature increased, the correlation weakened ($r \approx -0.95$ in convex), reflecting greater interface heterogeneity and complex field distortion.

Together, these results illustrated that both the magnitude and phase of impedance were highly sensitive to electrode geometry, not simply due to projected area but also due to mechanical conformity and contact quality—factors that should be carefully considered in the design of flexible, embedded electrode systems.

To contextualize the performance of the electrode line, all configurations were compared against a baseline ground truth impedance measurement, acquired by directly inserting the LCR meter's probes into the agar phantom. This setup provided an idealized, minimal-impedance interface, free from the geometric distortions and interface complexities introduced by embedded flexible electrodes. It served as a performance ceiling to assess how much deviation arose from the electrode architecture itself.

Figures A.8 - A.11 show Bode plots from the raw experimental data collected after calibration using the electrode line, the ground truth measurements, as well as

visual correlation plots per trial.

Across all geometries and trials, the electrode line consistently exhibited a phase lag relative to the ground truth. While impedance magnitudes showed variable trends, the measured phase angles were systematically more negative across the spectrum. This discrepancy was most pronounced in the low to mid-frequency band, where interface dynamics and double-layer formation dominate the capacitive response.

Several factors likely contributed to this behavior:

- **Distributed Interface and Parasitics:** The electrode line consisted of multiple copper segments embedded within silicone tubing. This configuration could have introduced delays due to cumulative charge storage and impedance propagation along the extended electrode path—effects absent in the localized, point-contact ground truth measurements.
- **Mechanical Contact Limitations:** Unlike the LCR probes, which established uniform, direct contact with the agar, the flexible electrode line—particularly in curved or embedded configurations—often experienced air gaps, nonuniform pressure, or partial exposure. These factors likely created local impedance discontinuities and distorted the electric field, contributing to additional capacitive lag.
- **Electrode Material Effects:** Copper, though highly conductive, is electrochemically less stable in aqueous or ionic media compared to noble metals like platinum or gold. It is more susceptible to surface oxidation and parasitic electrochemical reactions, which can alter both the double-layer capacitance and interfacial resistance. These effects are especially relevant at frequencies where surface kinetics dominate the impedance profile.

Taken together, these factors explain the more negative phase response observed in the electrode line compared to the ground truth. These findings underscore the importance of carefully interpreting EIS measurements from flexible, embedded systems and reinforce the need for circuit models that account for distributed, geometry-dependent, and interface-specific behaviors.

Given the emergence of curvature-dependent magnitude and phase shifts, I sought a physically grounded model that could capture both interfacial dynamics and bulk properties. The Lempka model [15], originally developed to describe EIS behavior

in neural electrodes, was well-suited for this purpose. It offers a physiologically interpretable structure: a CPE models non-ideal interface capacitance, a parallel resistance and CPE branch captures polarization behavior, and an additional series resistance reflects tissue and solution contributions. This separation of components allowed us to fit the observed data in a meaningful way, relating parameter changes directly to underlying physical mechanisms—such as current asymmetry, contact heterogeneity, and time constant compression—without overfitting to surface-level impedance variations.

5.4 Equivalent Circuit Modeling

5.4.1 Parameter Trends Across Geometries

To quantitatively analyze curvature-dependent impedance behavior, the experimental data was fitted to the model proposed by Lempka et al. [15], where the overall impedance is represented by contributions from the electrode–electrolyte double-layer (CPE_e), bulk ionic resistance through the tissue (R_∞), charge transfer resistance and dispersion within the tissue ($\Delta R \parallel CPE_t$), and a fixed parasitic capacitance ($C_p = 20$ pF). Given the magnitude of the measured impedances ($\sim 400\ \Omega$), the parasitic capacitance had a negligible contribution over the frequency range tested and effectively acted as an open circuit. This ensured that the extracted parameters primarily described the electrode–electrolyte interface and the distributed resistive and capacitive effects of the surrounding medium. For each geometry, model parameters were optimized directly against the measured complex impedance spectra using the AdamW optimizer with a weighted soft-bound penalty to enforce physically reasonable ranges on all parameters. The loss function was defined as the root-mean-square error (RMSE) between the measured and simulated impedance, computed jointly on the real and imaginary components of the spectra. The resulting fitted parameter trends across the four geometries are summarized in Figure 5.5.

The fitted parameters revealed consistent trends across the four geometries, though the underlying mechanisms should be interpreted cautiously. For the electrode interface, the constant phase element magnitude Q_e was approximately 1.3×10^{-5} for the straight line, increased to 1.6×10^{-5} for the single loop, remained at 1.5×10^{-5}

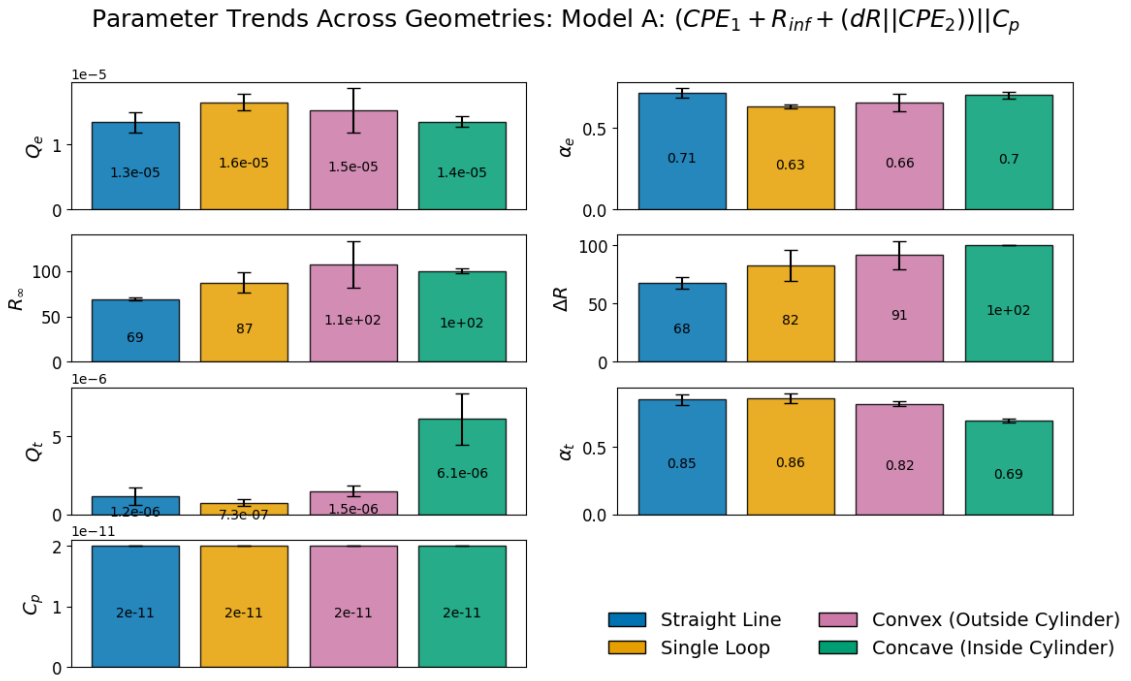

Figure 5.5: *Parameter trends across geometries*

for the convex wrapping, and then decreased slightly to 1.4×10^{-5} in the concave configuration. While one might expect the best mechanical contact (flat and concave) to correspond to the highest Q_e, the opposite was observed. This pattern suggests that Q_e does not scale purely with gross contact area but depends strongly on how the current density is distributed across the electrode surface. A likely explanation is that in geometries with partial lift-off, the uneven interface gives rise to localized regions of intense contact that act as hotspots for current injection, which enhance the apparent interfacial capacitance. By contrast, when contact is more uniformly distributed, as in the flat and concave geometries, the current is more evenly spread across the electrode, reducing such localized amplification and resulting in slightly lower Q_e.

The exponent α_e associated with this interfacial branch displayed a complementary trend: it remained relatively high for the straight and concave cases (0.71 and 0.70, respectively) and dropped for the single loop and convex configurations (0.63 and 0.66). This behavior likely reflects how heterogeneity in the mechanical interface and local field distribution, particularly in more curved cases, broadens the range of time

constants and leads to less ideal capacitive behavior. It is important to note that although curvature drove a more resistive global response in the raw data (as reflected in the in-plane curvature test), the circuit modeling shows that this resistive shift coexists with localized current hotspots that manifest as a higher fitted Q_e but with a lower α_e. In other words, the model parameters capture the increased heterogeneity of the interface, while the net effect observed in the raw spectra remains a loss of overall capacitive dominance.

The bulk series resistance R_∞, which dominates at high frequencies, rose from 69 Ω in the flat configuration to 87 Ω for the single loop, 110 Ω for the convex configuration, and 100 Ω for the concave configuration. These increases are linked to the effect of geometric curvature on the available conduction pathways. Increased curvature introduces longer and less direct current paths and reduces effective cross-sectional area, while any partial lift-off adds additional constriction. Even in the concave configuration, where lift-off appears to be minimized, the increased path lengths still contribute to a modest increase in R_∞.

$\Delta R \parallel CPE_t$ described delayed or distributed resistive behavior within the medium together with non-ideal capacitive dispersion caused by heterogeneity of the tissue-like environment and the spreading of field lines. Across the four geometries, ΔR increased from 68 Ω in the straight configuration to 82 Ω for the single loop, 91 Ω for the convex wrapping, and 100 Ω in the concave arrangement. These changes reflect how curvature alters the way current penetrates into the bulk medium: in curved geometries the electric field becomes more confined, so that the effective paths for ionic conduction become longer and more distributed. This effect is most pronounced in the concave case, where the electrode is well seated mechanically, but the surrounding cavity restricts the lateral spread of field lines and forces current to flow through narrower and more tortuous paths.

The parameters of CPE_t exhibited similar geometry dependence. The magnitude Q_t was relatively small in the straight (1.2×10^{-6}), single loop (7.3×10^{-7}), and convex (1.5×10^{-6}) cases, but increased substantially to 6.1×10^{-6} in the concave case. This rise indicates that the tighter field confinement within the cavity enhances capacitive storage within the bulk medium. Meanwhile, α_t remained close to 0.85–0.86 for the straight and looped geometries and 0.82 for the convex case, but fell sharply to 0.69 in the concave configuration, which suggests a broader distribution of relaxation times

at low frequencies as a result of this same confinement. The trends in ΔR, Q_t, and α_t point toward a progressive increase in distributed resistive and capacitive effects as the geometry restricts the spatial spread of the current.

Together, these parameter trends demonstrate that interface uniformity and contact pressure primarily influence the interfacial parameters Q_e and α_e, while geometric effects such as curvature and field confinement play a stronger role in shaping R_∞, ΔR, Q_t, and α_t. These findings emphasize that good conformity alone does not guarantee a simple impedance response: even in well-seated configurations, such as concave geometries, the three-dimensional geometry of the interface imposes strong effects on how current enters and disperses in the medium, producing electrical behavior shaped as much by field geometry as by contact mechanics.

5.4.2 Nyquist Fits

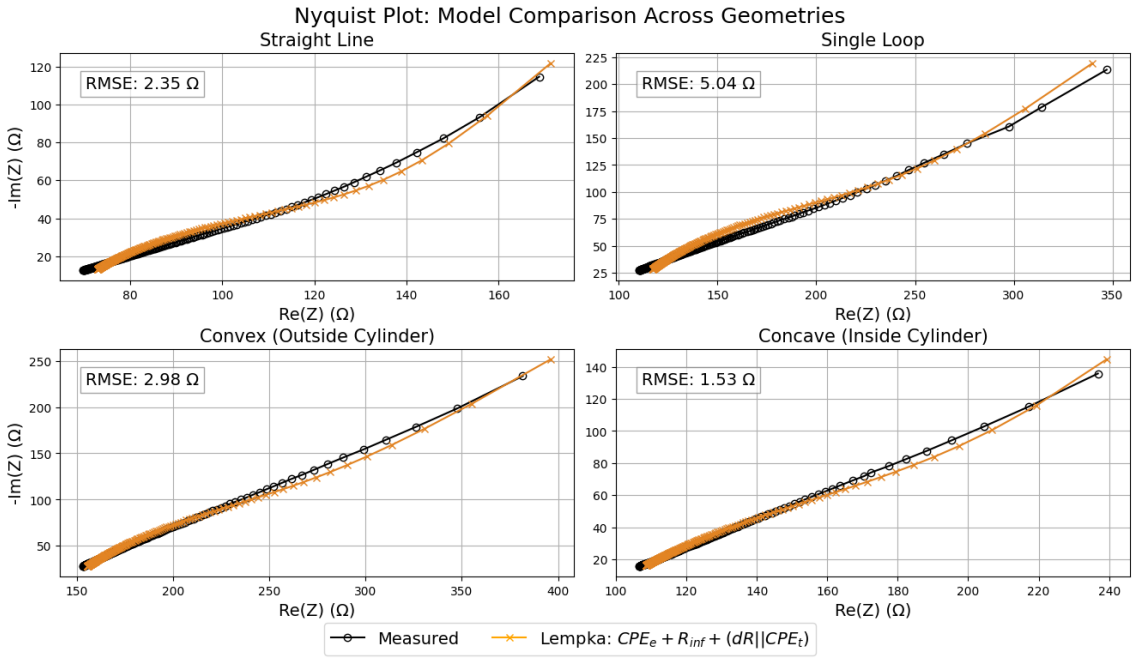

Figure 5.6: *Nyquist plots comparing measured impedance spectra to equivalent circuit model fits across different electrode geometries.*
Each subplot shows the average impedance response (black circles) for a representative trial of the soft electrode line in four configurations, with the RMSE values reported on the top left of each subplot.

The Nyquist plots (Figure 5.6) provided a direct comparison between the measured impedance spectra and the fitted responses of the original Lempka model across all four geometries. In the straight-line configuration, the model followed the measured data closely, producing a smooth, compact depressed arc-shaped trajectory consistent with the response of the $\Delta R \parallel \mathrm{CPE}_t$ branch in the high-frequency region and yielding a low fitting error (2.35 Ω). The single-loop case showed a visibly larger deviation between the measured and fitted curves, particularly at the low-frequency end where the measured arc extended further upward than predicted by the model, leading to the largest RMSE among the four cases (5.04 Ω). The convex configuration exhibited a similar pattern to the single loop, with the fitted response shifted along the real axis and a moderate fitting error (2.98 Ω). By contrast, the concave configuration yielded the best overall agreement, with the fitted curve closely overlapping the measured data throughout the entire frequency range and an RMSE of 1.53 Ω, even though this configuration introduced strong curvature.

The fits show that the model is able to reproduce the characteristic depressed semicircular arcs that dominate the high-frequency impedance spectra across all geometries. The most significant mismatches occur at low frequencies for the single-loop and convex cases, where the broad dispersion in the data produces almost straight corves that the model cannot capture with the available parameterization. In contrast, the concave geometry generates a more reproducible spectral shape that is well described by the same model structure. Overall, the Nyquist fits indicate that the Lempka formulation captures the major features of the impedance spectra for all tested geometries, with the quality of fit depending strongly on how well the $\Delta R \parallel \mathrm{CPE}_t$ branch approximates the shape of the high-frequency arc. The concave and straight configurations show excellent agreement with the model, while the looped and convex cases exhibit systematic residuals that suggest the presence of additional dispersion not fully represented by the current model structure.

5.5 Limitations

Despite promising electrical performance across a wide range of geometries, the current design and modeling framework presents several limitations related to experimental interpretation, model fidelity, and physical correspondence of fitted parameters.

From a hardware standpoint, the electrode system was not electrically shielded or impedance-matched, leaving it susceptible to parasitic effects such as stray capacitance and unintended coupling between adjacent segments. These parasitics may have been exacerbated by lead geometry changes during wrapping, twisting, or manual placement. Additionally, variability in electrode–gel contact across trials introduces uncertainty in the effective double-layer interface area, which directly impacts capacitance estimation. The measurement environment (agar + saline) was treated as homogeneous, yet changes in ion mobility near highly curved or recessed electrodes may have altered local impedance in ways not captured by the model.

The main interpretive challenge in using the original Lempka model lies in the way its constant phase elements (CPEs) serve as lumped approximations of non-ideal electrode interfaces and distributed conduction in the surrounding medium. While this compact representation can reproduce the overall shape of the impedance spectra, it inevitably compresses a wide range of frequency-dependent phenomena into a small number of elements. As a result, the fitted parameters can sometimes absorb effects that fall outside their natural frequency ranges, which makes it difficult to ascribe clear physical meaning to individual terms. Despite these limitations, the Lempka formulation was retained in this study because it captures the dominant features of the spectra with a small number of parameters and allows consistent comparisons across geometries, but it should be viewed as a simplified, lumped abstraction of inherently distributed electrochemical behavior rather than a fully descriptive physical model.

The equivalent circuit framework, while a useful tool, has inherent limitations when applied to soft, deformable electrode systems. The lumped-element approach cannot capture continuous spatial variation in impedance that arises from gradual curvature or deformation along the electrode line. Consequently, curvature-induced changes in impedance may be distributed among multiple circuit components in ways that do not uniquely correspond to specific physical processes. While extended models address this to some extent by introducing distributed ladder networks, these improvements come at the cost of increased model complexity and potential parameter coupling.

Finally, the fitting process itself can yield multiple parameter sets that reproduce the experimental impedance equally well, but imply different underlying physics.

Without external constraints or independent measurements (e.g., direct estimation of electrode surface area or parasitic capacitance), the allocation of spectral features to specific elements remains somewhat arbitrary. This limits the generalizability of fitted trends and complicates efforts to unambiguously link geometry, material properties, and operating conditions to specific circuit behaviors.

In total, while the model captures geometry-induced impedance trends with reasonable fidelity, the limitations discussed above underscore the need for more constrained, physically informed approaches. Future work should incorporate spatially resolved models, together with calibration and validation procedures, to isolate parasitic effects and ensure that fitted parameters correspond directly to physical mechanisms. These refinements will be essential for developing models that generalize across materials, geometries, and operating environments.

Chapter 6

Conclusions and Future Work

6.1 Conclusions

This work presents a soft, linearly distributed electrode array designed to remain functional across diverse geometries and mechanical loading conditions. Through systematic mechanical analysis and phantom-based impedance testing, I show that the electrode's electrical performance is intimately linked to its physical deployment state. Bending and load are not merely passive conditions but active modifiers of electrode–medium coupling, significantly altering the impedance response. These effects arise from predictable physical mechanisms—such as reduced contact area, increased interface resistance, and changes in local field distribution—and are captured only through models that explicitly account for distributed parasitics and low-frequency dispersion.

The mechanical analysis reveals that while the outer tubing and electrode materials remain highly compliant, the embedded stainless steel wire imposes a hard constraint on achievable curvature (1 cm) under safe contact force. The plastic deformation of the wires occurs at a bend radius of 2 cm. This insight helps define deployment limits and points to concrete design strategies for improvement, such as replacing the wire with a more compliant conductor or modifying the architecture to distribute strain more effectively. In practice, the interplay between stiffness and shape dictates where and how this system can be used—underscoring the need to evaluate mechanical design in tandem with electrical behavior.

On the electrical side, I found that simplified models often obscure key trends, particularly under conditions of high curvature or poor contact. By using the model proposed by Lempka et al. [15], I recover physically meaningful parameter trends that align with known electrochemical theory. These results not only validate the modeling approach but also highlight the value of fitting models that reflect the spatial and mechanical realities of soft electrode systems. In doing so, this work moves toward a more integrated understanding of how deformation affects measurement quality—beyond just surface conformity.

6.2 Future Work

6.2.1 Material and Fabrication Enhancements

The current electrode line leverages bare copper as the active conductive interface, which, while convenient and conductive, is prone to oxidation and can exhibit mechanical stiffness that compromises conformity. Future iterations of the device could benefit from using alternative electrode materials or coatings that maintain electrical performance under bending. Platinum black or gold-plated surfaces are standard in clinical devices and could offer superior biocompatibility, lower impedance, and resistance to degradation. Conductive polymer coatings such as PEDOT:PSS are another promising avenue—they can conform to microgeometry changes during bending and maintain contact despite mechanical mismatch. In addition, the mechanical limitations introduced by the stiff stainless steel wire could be alleviated by replacing it with superelastic materials such as nitinol, or by adopting stiffness tunable materials. Such redesigns would expand the deployable curvature range while reducing contact force and mechanical risk.

6.2.2 Experimental Setup Improvements

Several improvements to the experimental protocol would help isolate and better interpret the electrical behavior of the electrode system. Using a gel-based or fully submerged electrolyte environment would minimize variability due to air exposure or inconsistent immersion depth, which currently confound impedance measurements

under curvature. A well-controlled setup could employ jigs that enforce known curvature while maintaining constant electrolyte contact. Future tests should also implement a four-electrode EIS setup, decoupling interface impedance from measurement lead impedance and improving signal fidelity. Surface contact mapping—via imaging, pressure-sensitive film, or micro-CT—would offer quantitative data on actual electrode–phantom contact area, enabling correlation with impedance changes and validation of surface-driven modeling assumptions.

6.2.3 Advanced Modeling and Simulation

The present study used lumped-element models to describe the impedance behavior under curvature and load. While this approach yields useful insight, it assumes spatially homogeneous impedance distributions. Future work should incorporate distributed models—such as finite element simulations—that spatially resolve how contact quality varies along the electrode line and substrate. This would allow modeling of partial or segmented contact conditions typical of curved deployments. Incorporating priors from physical measurements, such as fixed measured parasitic capacitance or estimated contact areas, would also regularize parameter fits and reduce compensatory artifacts. Additionally, integrating real geometry and material properties into an FEA model would enable full electromechanical co-simulation, illuminating how deformation directly modulates local impedance distributions. Such physics-informed modeling could guide both circuit design and fabrication strategies.

6.2.4 Expanded Validation and Application Testing

To build a generalizable understanding of the electrode's performance, broader validation across geometries, frequencies, and mechanical states is essential. Future experiments should systematically vary curvature in finer increments and combine it with graded contact pressures. This would enable continuous mapping of impedance as a function of mechanical state and facilitate data-driven interpolation or predictive modeling. Beyond mechanical deformation, testing in more realistic biological environments—such as ex vivo tissues or dynamic phantoms with time-varying motion—would reveal how the electrode performs under conditions that mimic clinical deployment. Repeatability studies across multiple fabrication batches would assess

manufacturing robustness. Finally, long-term stability testing could uncover whether mechanical stress leads to hysteresis, delamination, or performance drift, which are key factors for real-world implementation.

6.2.5 Toward Embedded Sensing and Soft Robotics Integration

Ultimately, the electrode line is envisioned as part of a broader class of conformable, deployable biosensing systems for soft robotics and medical applications. To support this goal, future work should explore embedding these electrodes into reconfigurable substrates—such as soft actuators or deployable structures—that can self-position inside the body or around an object. Integration with on-board electronics for wireless readout, signal amplification, or multiplexing could enable fully autonomous operation in confined or in vivo environments. Embedding strain or temperature sensors alongside the impedance electrodes would open the door to multimodal feedback systems for adaptive mapping or closed-loop control. This trajectory would transform the electrode line from a passive sensing element into a component of intelligent, body-conforming robotic systems.

Appendix A

Appendix

A.1 Electrode Line

Figure A.1: *Full electrode line in three different configurations.*

A.2 Calibration

Inner to outer electrode resistances were measured per electrode on the LCR meter and the average values over 3 trials were used in all calculations. Electrode 19 showed broken contact due to epoxy delamination and was not included in any measurements or analysis. Most resistances were found to be under 10Ω, as can be seen in Figure A.2. Variations can be attributed to the thinning of the epoxy from the rolling during fabrication. These values were then summed with the wire resistances to be used for calibration.

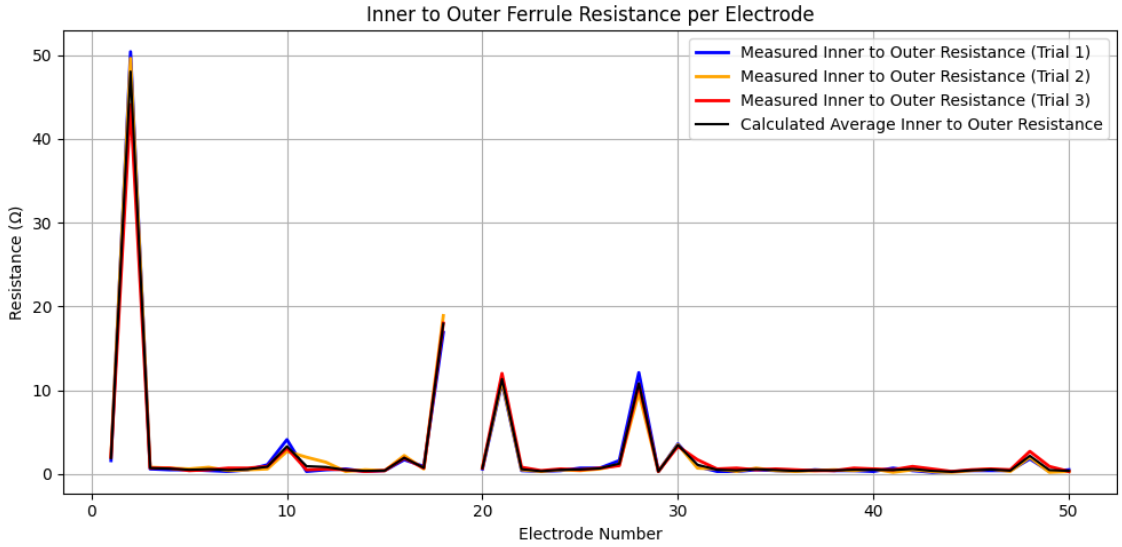

Figure A.2: *Inner to outer electrode resistances per electrode.*

A.3 Phantom Geometries and Molds

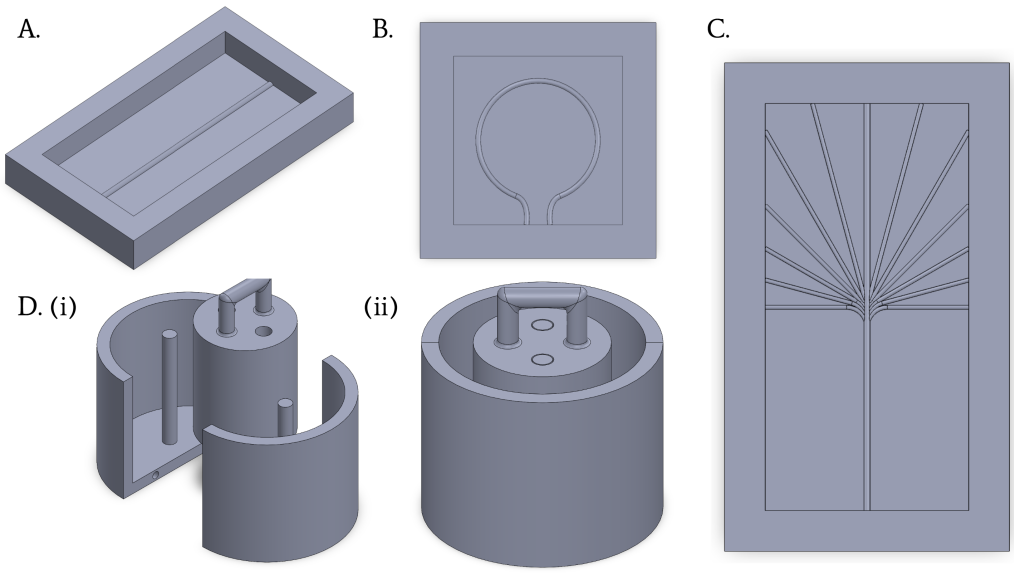

Figure A.3: *CAD models for phantom mold fabrication.*
A. Mold for straight line (2D) geometry. B. Mold for single loop (2D) geometry. C. Mold for angular curvature tests (2D). D. Three-part mold assembly for cylindrical (3D) geometries: (i) exploded view (ii) assembled view.

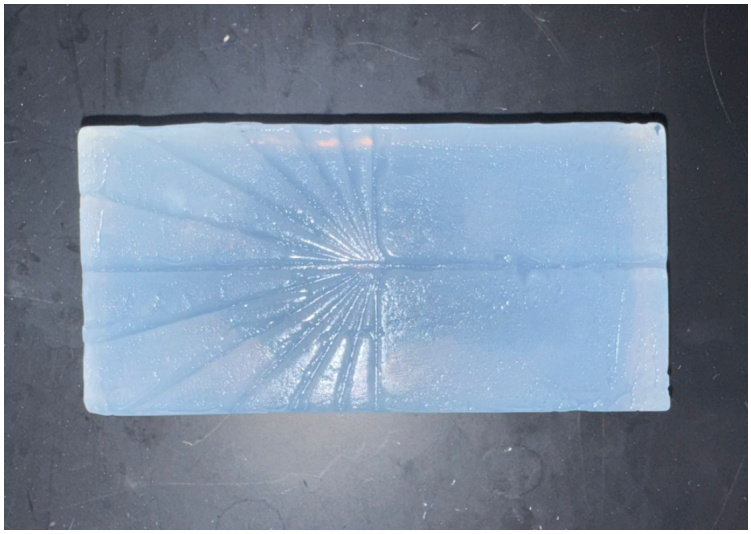

Figure A.4: *NaCl-Agar phantom for in-plane angular curvature test.*

A.3.1 Convex vs. Concave Geometry

Feature	Convex (Outward-Wrapped)	Concave (Inward-Placed)
Electrode Configuration	Electrode is wrapped externally along the outer surface of a curved cylinder	Electrode is placed inside a cylindrical cavity, conforming along the inner surface
Mechanical Support	Electrode resists curvature; no physical boundaries assist conformity	Cavity walls provide passive mechanical support, promoting conformity
Strain on Electrode	Bending induces tension along outer arc; can resist placement	Compression-dominant; less strain needed to maintain position
Risk of Lift-off or Buckling	Moderate to high; edges can lose contact if curvature is severe or material is stiff	Minimal; cavity enforces contact through wire stiffness and geometric confinement
Contact Stability	Dependent on external pressure or adhesive support	Intrinsically stabilized by cavity shape and electrode weight
Electric Field Uniformity	Field lines may become distorted due to partial detachment or inconsistent contact	More symmetric field distribution due to better conformity and alignment
Sensitivity to Pressure	External pressure is often necessary to enhance conformity and reduce impedance	Geometry provides passive pressure; added weight further enhances contact
Expected Electrical Impedance Trends (Qualitative)	May show elevated impedance due to poor contact, especially at low frequencies	Tends to exhibit lower and more stable impedance from improved electrode-media coupling

Table A.1: *Comparison of Convex and Concave Phantom Geometries: Mechanical and Electrical Considerations.*

A.4 Finite Element Analysis

A.4.1 Overview

Finite element analysis (FEA) was conducted to investigate the bending mechanics and potential failure modes of the linear electrode device. The primary objectives of this study were:

- To quantify the moment–curvature relationship of the electrode and compare it against analytical estimates presented in the main text.
- To evaluate the likelihood of mechanical or interfacial failure under bending loads by modeling stresses and strains throughout the structure.

This analysis focused on the epoxy-tubing-electrode composite structure. The stainless steel wire was not explicitly modeled because its regular geometry and well-established material properties were adequately addressed through analytical solutions.

A.4.2 Methods

A three-dimensional FEA model was developed in *ANSYS 2025R1*. The model represented a short, symmetric segment of the electrode device subjected to pure bending.

Symmetry planes were applied about both the longitudinal and transverse axes to reduce computational cost. A bending moment was applied at one end of the model while corresponding degrees of freedom on the opposite planes were constrained as shown in Figure A.5.

The model included three components: copper electrodes, silicone tubing, and an epoxy adhesive layer. Characteristic mesh sizes were 0.2 mm for the electrodes, 0.2 mm for the tubing, and 0.02 mm for the epoxy in high-stress regions. The mesh was composed of approximately 106,475 elements, comprising:

- 106,568 TET10 elements (10-node quadratic tetrahedral),
- 1,714 HEX20 elements (20-node quadratic hexahedral),
- 76 PYRAMID13 elements (13-node wedge).

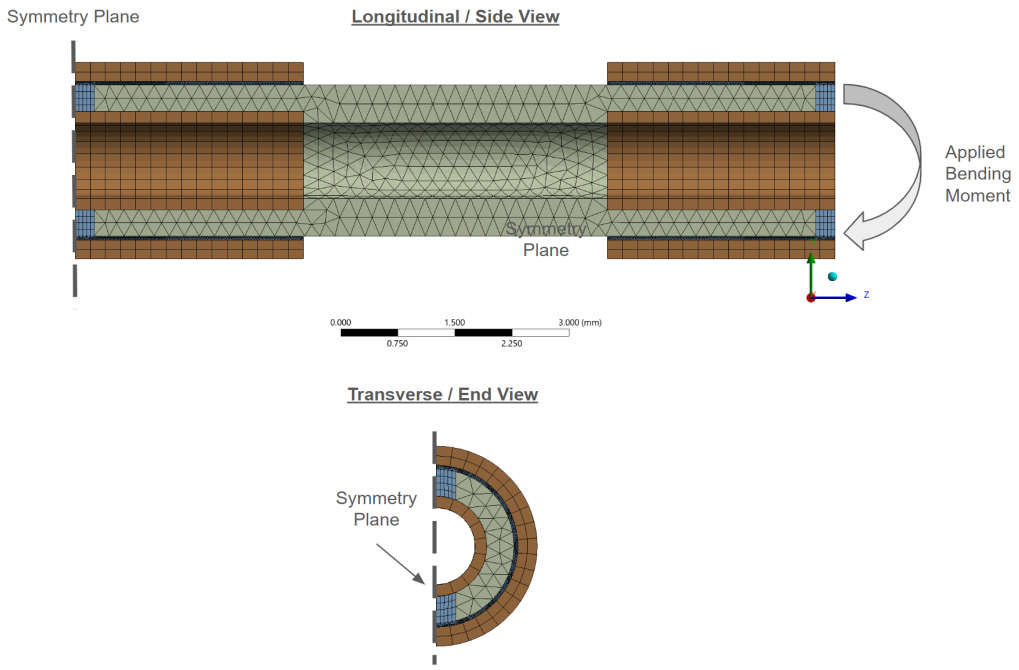

Figure A.5: *Refined model showing geometry, symmetry planes, and loading conditions.*

All materials were modeled as isotropic and linear elastic. Nonlinear geometric effects were included in the solution. Interfaces between materials were modeled as perfectly bonded. Material properties used in the simulations are summarized in Table A.2.

Part	**Material**	**Young's Modulus**	**Poisson's Ratio**
Electrodes	Copper	110 GPa	0.30
Tubing	Silicone (average)	1 MPa	0.40
Adhesive	Silver epoxy (MG 8331S)	760 MPa	0.40

Table A.2: *Material properties used for FEA.*

The analysis was conducted in two stages:

1. **Moment–Curvature Analysis**: A coarse-mesh model was used to extract the bending moment–curvature relationship across a range of applied curvatures.
2. **Failure Mode Analysis**: The critical bending moment obtained from the first stage was applied to a refined mesh focused on the bonded regions, in order to

resolve interfacial stresses and strains.

Potential failure mechanisms considered included:

- Interfacial bond failure at the epoxy-tubing and epoxy-electrode interfaces (via interfacial shear stress).
- Intra-adhesive failure of the epoxy material itself.
- Strain or stress limits of the silicone tubing and epoxy material.

A.4.3 Results

Moment–Curvature Relationship

The simulated moment–curvature response is shown in Figure A.6. At low curvature values, the relationship was approximately linear with a slope of 1.27 N·mm^2. Beyond a curvature of about 0.07 mm^{-1}, the response became nonlinear. A bending moment of approximately 6.35×10^{-2} N·mm was required to generate a curvature of 0.05 mm^{-1}, corresponding to a 20 mm bend radius.

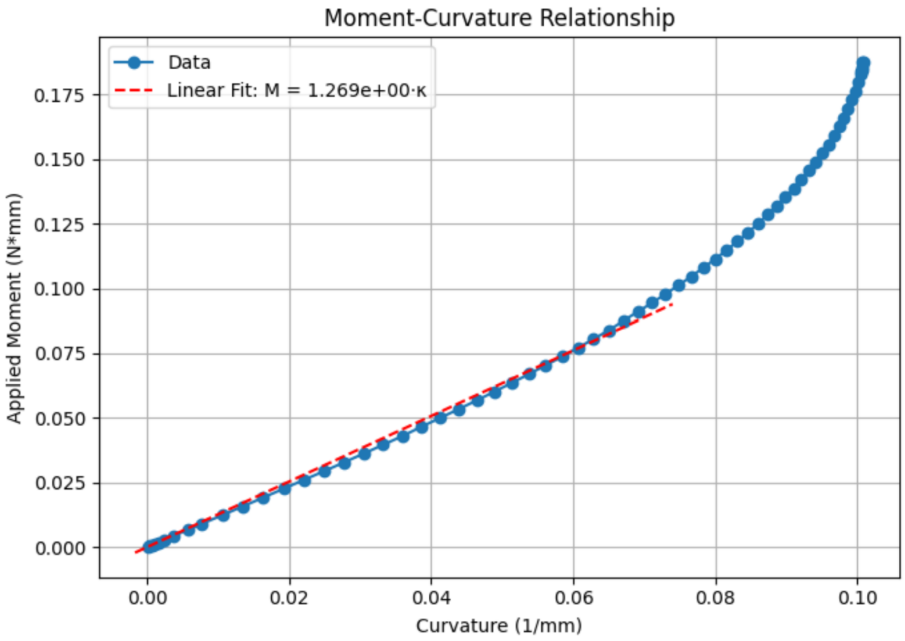

Figure A.6: *Bending moment vs. curvature.*

Stress and Strain Fields

The critical bending moment identified above was then applied to a refined model with a finer mesh near the bonded interfaces. Peak stresses and strains were observed at the leading edge of the epoxy-tubing interface, as shown in Figure A.7.

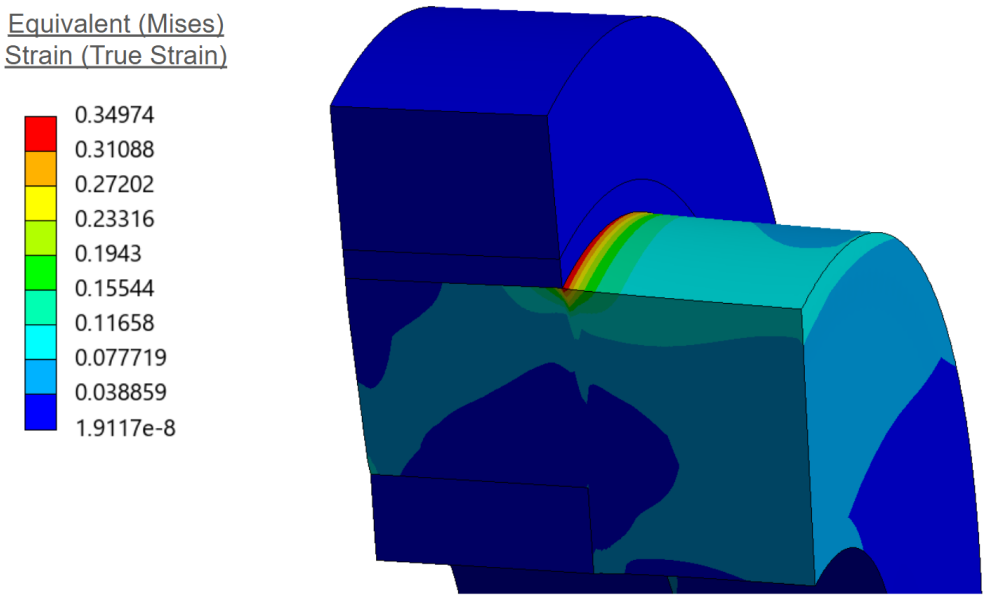

Figure A.7: *Strain contours showing localization of peak stresses at the epoxy-tubing interface.*

Key findings from this analysis are summarized in Table ??. Maximum tubing strain reached 34.1%, well below the approximate 700% failure strain of silicone. Epoxy strain was limited to 0.19%, below its 5.3% limit. However, interfacial shear stresses at the epoxy-tubing interface reached 1.76 MPa, which exceeds estimated bond strengths, indicating a likelihood of debonding during repeated bending. Stresses at the epoxy-electrode interface remained below their estimated strength.

A.4.4 Discussion

The FEA results showed that peak stresses and strains were localized near the leading edge of the epoxy–tubing interface, where bending introduces shear and peeling forces

Failure Mode	Max Value	Threshold	Concern?
Epoxy strain	0.19 mm/mm	5.3%	No
Tubing strain	34.1 mm/mm	700%	No
Epoxy-tubing interface shear stress	1.76 MPa	∼0.1 MPa	Yes
Epoxy-electrode interface shear stress	0.28 MPa	∼1 MPa	No

Table A.3: *Computed maximum values for key failure modes.*

at the bonded region. This stress concentration occurred in a small, localized zone and did not extend into the main body of the adhesive or tubing. Importantly, the regions around the access holes (used for electrical contact) remained intact throughout the simulated deformation, suggesting that the structural integrity of these holes is maintained and that the electrical performance of the device would not be disrupted by bending.

While the simulations revealed stress localization, it is important to recognize that the model employed idealized constraints. In reality, the epoxy is partially overconstrained by the surrounding ferrule geometry, which helps prevent excessive peeling and spreads the applied bending load more symmetrically along the interface. Under realistic deployment conditions, bending would be distributed along the length of the bonded region, reducing the risk of catastrophic local failure compared to the idealized, concentrated moment loading applied in this simulation.

Several broader insights can be drawn from this analysis:

- The most critical limitation of the device lies at the epoxy–tubing interface rather than in the bulk properties of the materials.
- Although the tubing and epoxy materials tolerate significant elastic deformation, the adhesion between these materials is relatively weak, making it a priority area for improvement in future iterations (e.g., via primers or surface treatments).
- These findings remain subject to uncertainties in material properties and modeling assumptions, particularly for soft polymers like silicone, which vary considerably by formulation.
- The press-fit assembly of the inner electrode is expected to introduce slight deformation of the tubing outer diameter, which in turn reduces the adhesive layer thickness. This effect could elevate interfacial stresses beyond the predictions

of the simplified model and should be accounted for in future refinements.

- Application-specific designs should include more detailed property characterization (including interfacial strength), finer mesh studies, and symmetric boundary conditions that more accurately reflect in-use deployment.

For the purposes of this proof-of-concept study, these analyses were deemed sufficient to identify key mechanical vulnerabilities and demonstrate that, under normal operation, structural integrity at the access holes and electrical continuity are unlikely to be compromised, while the primary risk remains concentrated at the epoxy–tubing interface.

A.5 Impedance Measurements Across Geometries: Trial Data

Figures A.8 through A.11 show the impedance-frequency response and corresponding magnitude–phase relationship across three trials for each electrode line configuration. For each trial, the top two rows plot the mean impedance magnitude and phase across frequency, with individual electrode pair responses in grey, the mean in black, ±1 standard deviation in dashed red, and ground truth in dashed blue. The bottom row illustrates the correlation between mean impedance magnitude and phase across frequencies.

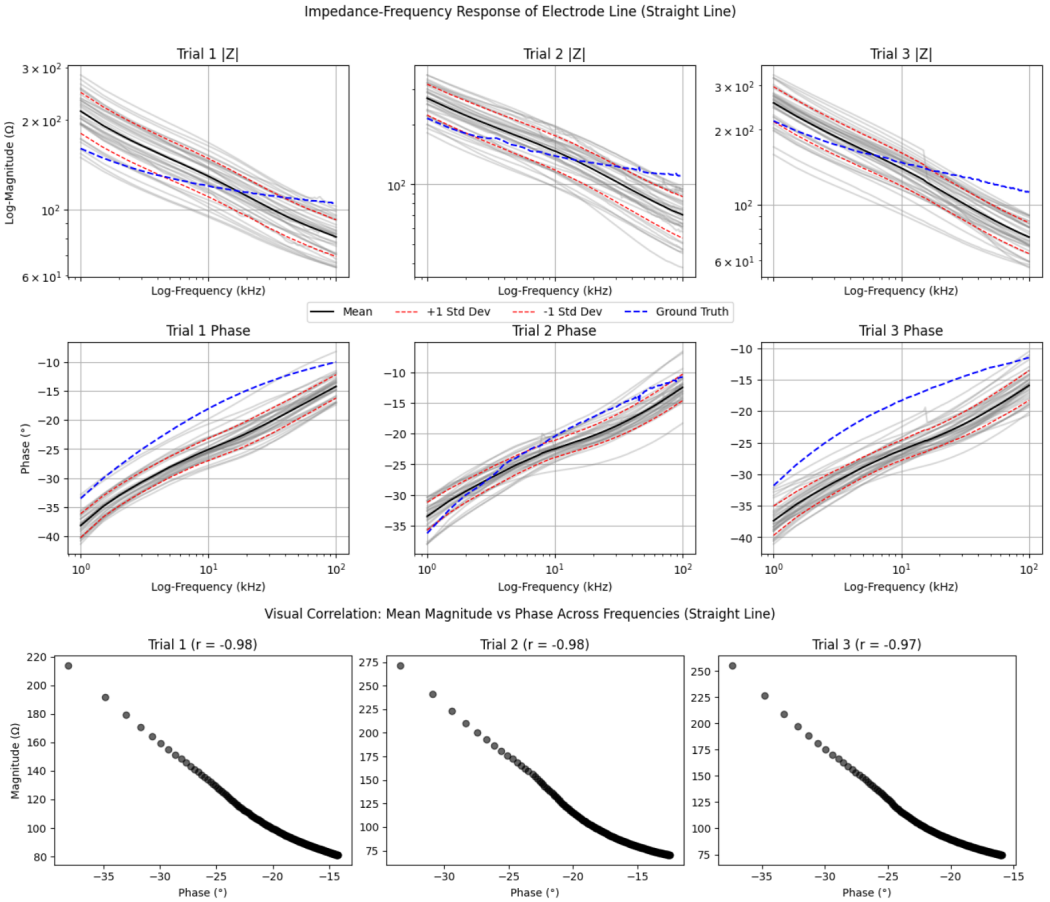

Figure A.8: *Impedance response and magnitude-phase correlation per trial for straight line configuration.*

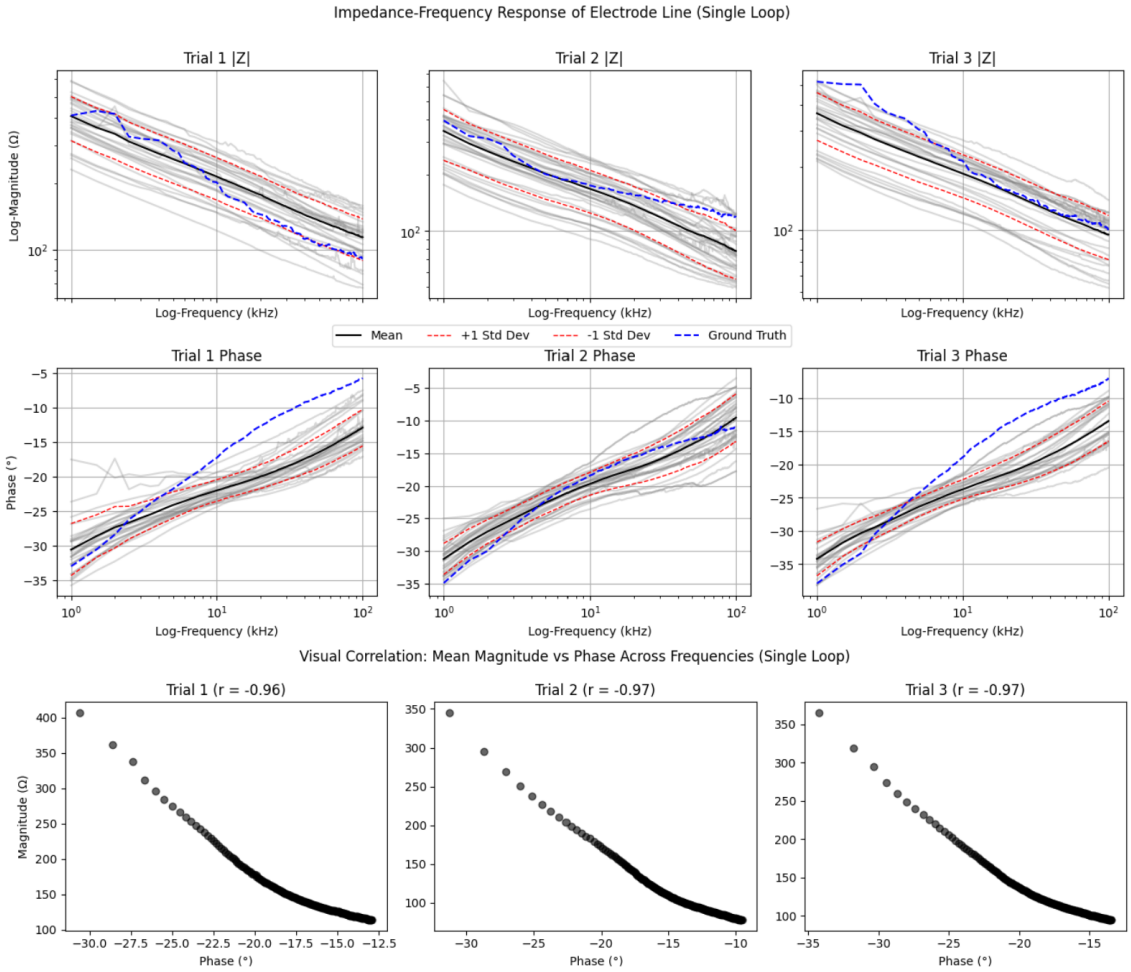

Figure A.9: *Impedance response and magnitude-phase correlation per trial for loop configuration.*

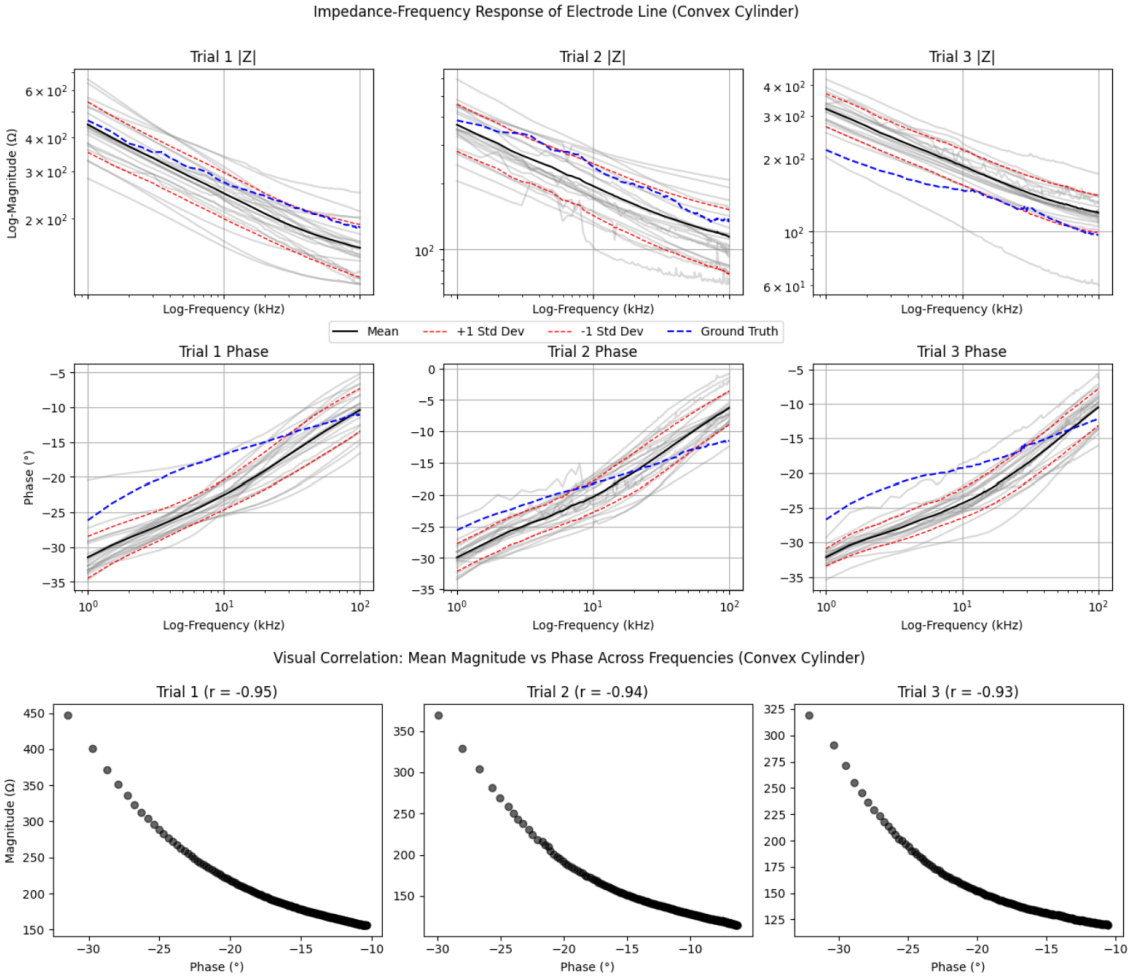

Figure A.10: *Impedance response and magnitude-phase correlation per trial for convex configuration.*

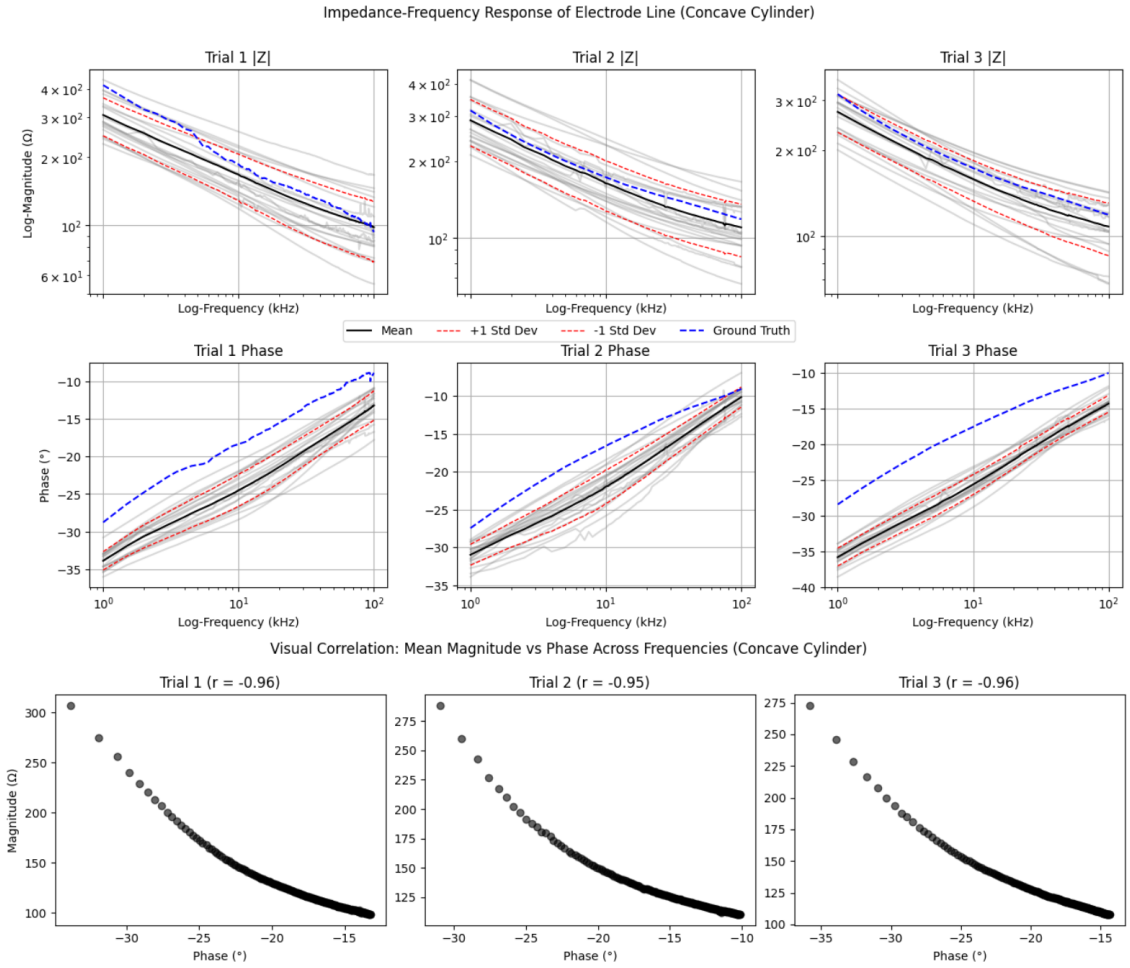

Figure A.11: *Impedance response and magnitude-phase correlation per trial for concave configuration.*

Bibliography

[1] Riaz Ahmed and Kenneth Reifsnider. Study of influence of electrode geometry on impedance spectroscopy. In *International conference on fuel cell science, engineering and technology*, volume 44052, pages 167–175, 2010. 1.2.3

[2] Awaz Ali, Aimee Sakes, Ewout A Arkenbout, Paul Henselmans, Remi van Starkenburg, Tamas Szili-Torok, and Paul Breedveld. Catheter steering in interventional cardiology: Mechanical analysis and novel solution. *Proceedings of the Institution of Mechanical Engineers, Part H: Journal of Engineering in Medicine*, 233(12):1207–1218, 2019. 1.2.1

[3] Elisa Azzarello, Elisa Masi, and Stefano Mancuso. Electrochemical impedance spectroscopy. In *Plant electrophysiology: Methods and cell electrophysiology*, pages 205–223. Springer, 2012. 1.1, 1.2.1

[4] Stuart F Cogan. Neural stimulation and recording electrodes. *Annu. Rev. Biomed. Eng.*, 10(1):275–309, 2008. 1.1, 1.2.3

[5] Robert Daly, Tarun Narayan, Alan O'Riordan, and Pierre Lovera. Platinum interdigitated electrode arrays for reagent-free detection of copper. 2021. 1.2.1

[6] Huazhi Dong, Sihao Teng, Xiaopeng Wu, Xu Han, Francesco Giorgio-Serchi, and Yunjie Yang. Flexible electrical impedance tomography for tactile interfaces. *arXiv preprint arXiv:2411.13306*, 2024. 1.2.1

[7] Yavuz Nuri Ertas, Derya Ozpolat, Saime Nur Karasu, and Nureddin Ashammakhi. Recent advances in cochlear implant electrode array design parameters. *Micromachines*, 13(7):1081, 2022. 1.2.1

[8] Wendy Franks, Iwan Schenker, Patrik Schmutz, and Andreas Hierlemann. Impedance characterization and modeling of electrodes for biomedical applications. *IEEE Transactions on Biomedical Engineering*, 52(7):1295–1302, 2005. 1.1, 1.2.3

[9] Shu Gong, Willem Schwalb, Yongwei Wang, Yi Chen, Yue Tang, Jye Si, Bijan Shirinzadeh, and Wenlong Cheng. A wearable and highly sensitive pressure sensor with ultrathin gold nanowires. *Nature communications*, 5(1):3132, 2014. 1.1

[10] Mengdi Han, Lin Chen, Kedar Aras, Cunman Liang, Xuexian Chen, Hangbo Zhao, Kan Li, Ndeye Rokhaya Faye, Bohan Sun, Jae-Hwan Kim, et al. Catheter-integrated soft multilayer electronic arrays for multiplexed sensing and actuation during cardiac surgery. *Nature biomedical engineering*, 4(10):997–1009, 2020. 1.2.2

[11] Ya Huang, Kuanming Yao, Jiyu Li, Dengfeng Li, Huiling Jia, Yiming Liu, Chun Ki Yiu, Wooyoung Park, and Xinge Yu. Recent advances in multi-mode haptic feedback technologies towards wearable interfaces. *Materials Today Physics*, 22:100602, 2022. 1.1, 1.2.1

[12] Madhuvanthi A Kandadai, Jason L Raymond, and George J Shaw. Comparison of electrical conductivities of various brain phantom gels: Developing a 'brain gel model'. *Materials Science and Engineering: C*, 32(8):2664–2667, 2012. 1.1, 3.1

[13] Yeo Kenry. Jc, & lim, ct (2016). emerging flexible and wearable physical sensing platforms for healthcare and biomedical applications. *Microsystems Nanoengineering, Nature*, 2:16043. 1.1, 1.2.2

[14] Eun Kwang Lee, Ratul Kumar Baruah, Hansraj Bhamra, Young-Joon Kim, and Hocheon Yoo. Recent advances in electrode development for biomedical applications. *Biomedical Engineering Letters*, 11:107–115, 2021. 1.1

[15] Scott F Lempka, Svjetlana Miocinovic, Matthew D Johnson, Jerrold L Vitek, and Cameron C McIntyre. In vivo impedance spectroscopy of deep brain stimulation electrodes. *Journal of neural engineering*, 6(4):046001, 2009. (document), 1.1, 1.2.3, 1.3, 5.3, 5.4.1, 6.1

[16] Kyeonghee Lim, Hunkyu Seo, Won Gi Chung, Hayoung Song, Myoungjae Oh, Seoung Young Ryu, Younhee Kim, and Jang-Ung Park. Material and structural considerations for high-performance electrodes for wearable skin devices. *Communications Materials*, 5(1):49, 2024. 1.1, 1.2.2

[17] Liu D Liu, Susu Chen, Han Hou, Steven J West, Mayo Faulkner, Michael N Economo, Nuo Li, Karel Svoboda, et al. Accurate localization of linear probe electrode arrays across multiple brains. *ENeuro*, 8(6), 2021. 1.2.1

[18] Roberto Merletti, Dario Farina, and Marco Gazzoni. The linear electrode array: a useful tool with many applications. *Journal of Electromyography and Kinesiology*, 13(1):37–47, 2003. 1.2.1

[19] Sanjiv M Narayan and Roy M John. Advanced electroanatomic mapping: current and emerging approaches. *Current Treatment Options in Cardiovascular Medicine*, 26(4):69–91, 2024. 1.1, 1.2.1

[20] Marc Ovadia and Daniel H Zavitz. The electrode–tissue interface in living heart: equivalent circuit as a function of surface area. *Electroanalysis: An International Journal Devoted to Fundamental and Practical Aspects of Electroanalysis*, 10(4):

262–272, 1998. 1.1, 1.2.3

[21] Roland Pomfret, Karl Sillay, and Gurwattan Miranpuri. Investigation of the electrical properties of agarose gel: characterization of concentration using nyquist plot phase angle and the implications of a more comprehensive in vitro model of the brain. *Annals of neurosciences*, 20(3):99, 2013. 1.1

[22] Guozhen Shen. Recent advances of flexible sensors for biomedical applications. *Progress in Natural Science: Materials International*, 31(6):872–882, 2021. 1.1

[23] Diana Vilela, Agostino Romeo, and Samuel Sánchez. Flexible sensors for biomedical technology. *Lab on a Chip*, 16(3):402–408, 2016. 1.1, 1.2.2

[24] Liu Wang, Chuan Fei Guo, and Xuanhe Zhao. Magnetic soft continuum robots with contact forces. *Extreme Mechanics Letters*, 51:101604, 2022. 1.2.1

[25] Pim W Weijenborg, Wout OA Rohof, Louis MA Akkermans, Joanne Verheij, André JPM Smout, and Albert J Bredenoord. Electrical tissue impedance spectroscopy: a novel device to measure esophageal mucosal integrity changes during endoscopy. *Neurogastroenterology & Motility*, 25(7):574–e458, 2013. 1.2.1

[26] Yuki Yamamoto, Shingo Harada, Daisuke Yamamoto, Wataru Honda, Takayuki Arie, Seiji Akita, and Kuniharu Takei. Printed multifunctional flexible device with an integrated motion sensor for health care monitoring. *Science advances*, 2(11):e1601473, 2016. 1.2.1

[27] Katsuaki Yokoyama, Hiroshi Nakagawa, Dipen C Shah, Hendrik Lambert, Giovanni Leo, Nicolas Aeby, Atsushi Ikeda, Jan V Pitha, Tushar Sharma, Ralph Lazzara, et al. Novel contact force sensor incorporated in irrigated radiofrequency ablation catheter predicts lesion size and incidence of steam pop and thrombus. *Circulation: Arrhythmia and Electrophysiology*, 1(5):354–362, 2008. 4.1

[28] Xiao-Zi Yuan, Chaojie Song, Haijiang Wang, and Jiujun Zhang. *Electrochemical impedance spectroscopy in PEM fuel cells: fundamentals and applications*, volume 13. Springer, 2010. 1.1, 1.2.3